A Parametric Level Set Approach to Simultaneous Object Identification and Background Reconstruction for Dual Energy Computed Tomography

Oguz Semerci and Eric L. Miller, *Senior Member, IEEE*

Abstract

Dual energy computerized tomography has gained great interest because of its ability to characterize the chemical composition of a material rather than simply providing relative attenuation images as in conventional tomography. The purpose of this paper is to introduce a novel polychromatic dual energy processing algorithm with an emphasis on detection and characterization of piecewise constant objects embedded in an unknown, cluttered background. Physical properties of the objects, specifically the Compton scattering and photoelectric absorption coefficients, are assumed to be known with some level of uncertainty. Our approach is based on a level-set representation of the characteristic function of the object and encompasses a number of regularization techniques for addressing both the prior information we have concerning the physical properties of the object as well as fundamental, physics-based limitations associated with our ability to jointly recover the Compton scattering and photoelectric absorption properties of the scene. In the absence of an object with appropriate physical properties, our approach returns a null characteristic function and thus can be viewed as simultaneously solving the detection and characterization problems. Unlike the vast majority of methods which define the level set function non-parametrically, i.e., as a dense set of pixel values), we define our level set parametrically via radial basis functions (RBF's) and employ a Gauss-Newton type algorithm for cost minimization. Numerical results show that the algorithm successfully detects objects of interest, finds their shape and location, and gives a adequate reconstruction of the background.

Index Terms

Computed tomography, dual-energy, polychromatic spectrum, parametric level set, inverse problems, iterative reconstruction

I. INTRODUCTION

A conventional computed tomography (CT) imaging system provides a reconstruction of the linear attenuation coefficient distribution of an object under investigation. Dual energy techniques, however, allow for more detailed

O. Semerci and E.L. Miller are with the Department of Electrical and Computer Engineering, Tufts University, Medford, MA, 02155 USA e-mail: elmiller@ece.tufts.edu.

chemical characterization of the material using measurements from two distinct X-ray spectra. These methods have been applied in a range of application areas including non-destructive material evaluation [1], medical imaging [2], cardiac and coronary imaging [3], bone densitometry [4] and airport/seaport security [5].

The dual energy idea was initially proposed by Alvarez and Macovsky [6] who modeled the total attenuation of X-rays as a linear combination photoelectric absorption and Compton scattering coefficients with corresponding empirical energy dependent basis functions. In detail, a cubic polynomial approximation of the polychromatic measurement models was used to estimate sinograms of photoelectric and Compton components. Once sinograms were estimated, the filtered back projection (FBP) algorithm was applied to obtain photoelectric and Compton coefficient reconstructions. The polynomial approximation, however, was found to be accurate only for test subjects whose properties were "close enough" to data subjects used to obtain the model coefficients. Also the sinogram estimation step amplified the noise leading to erroneous reconstructions especially for the photoelectric component [6]. Later, basis material decomposition methods, where attenuation coefficients of two or more materials constitute the basis set for the total attenuation, were proposed [7], [8]. For these methods, the reconstruction problem was reduced to estimation of the space-varying weight of each basis material. This approach is accurate when the properties in the materials of interest are, in a sense, "spanned" by the spectral characteristics of the basis material [9]. Optimal selection of the basis set is generally application dependent with a variety of approaches having been explored in the literature to date [10], [11], [12]. A review of the accuracy of these methods can be found in [12]. The methods where the estimation of sinograms of basis components is followed by FBP reconstructions of the corresponding images are referred as prereconstruction methods. Alternatively in the case of postreconstruction type of methods, filtered back projection is used to form separate attenuation images from the high and low energy projection data which are then mapped into basis material images [13], [1]. It is well-known that both of these conventional approaches to the dual energy problem have poor noise properties and are prone to inaccuracies in the measurement data as they use FBP [14], [15], [16].

In addition to reconstruction methods based on FBP, significant work has been directed toward the use of iterative image formation schemes for dual energy CT. Such methods provide the opportunity to more precisely take into account the nonlinear relationship between the data and the material properties than is afforded by FBP-based algorithms. Moreover, iterative techniques can be tailored to the underlying Poisson nature of the observations and provide a natural mechanism for incorporating prior information into the image formation process [17]. Within the context of dual energy CT, initial work on iterative methods focused on using the algebraic reconstruction technique (ART) and basis material decomposition for iterative beam hardening correction [18], [19]. More recently, iterative methods based on maximum likelihood and maximum *a posteriori* (MAP) statistical principles have been developed for monochromatic and polychromatic dual energy reconstruction problems [14], [16], [20] arising primarily in the medical imaging domain. Such methods have proven to be more accurate than previously proposed iterative and FBP based approaches especially in low photon count (i.e., low SNR) scenarios.

While medical applications have motivated a significant majority of algorithm development for dual energy CT, in recent years, there has been growing interest in the application of this imaging modality to problems in airport

and seaport security; specifically the screening of checked luggage [5], [21], [22], [23]. Unlike the medical imaging problem, the range of materials encountered in baggage screening is quite broad. As such, it remains an open question as to whether and how material basis-type decompositions of the attenuation coefficient can be applied in this context. Indeed, the state-of-the art here is represented by the work of Ying *et al.* who consider the recovery of the Compton and photoelectric coefficients directly in [5]. Following a similar approach to [6], Ying *et al.* employ a prereconstruction imaging scheme in which the sinograms for the photoelectric and Compton coefficients are obtained via the solution of a non-linear constrained optimization problem. As was the case in [6], high fidelity recovery of the photoelectric coefficient proved challenging due to the domination of the Compton effect relative to the photoelectric for this class of problems. Roughly speaking the signal to noise ratio associated with the photoelectric component was far smaller than that of the Compton making stable recovery of the former difficult.

Consideration of these issues associated with the use of dual energy CT for luggage screening provides the impetus for the work in this paper. To date, the algorithms developed for the screening problem are rather similar to those developed for medical applications despite the fact that the fundamental objectives of these two problems are somewhat different. In the medical case, the processing goal is the creation of high resolution images capable of supporting accurate diagnoses. For the security problem however, while one may still desire a good "picture," an additional goal is the determination as to whether a given object contains illicit materials and if so, how are they distributed. Such materials of interest will be embedded in an unknown and generally quite inhomogeneous background; however, prior information exists concerning the types of materials that may be of interest. Our approach to bringing this and related prior information to bear on the image formation process has not, to the best of our knowledge, been considered.

Motivated by these observation, in this paper we propose a variational approach to image formation adapted to the problem of detecting and characterizing "anomalies" in multiple physical parameters located in a cluttered and unknown environment. The contributions of this work are as follows. First we propose a new, hybrid model and associated inversion methods for the determination of the geometry and contrast associated with these anomalies along with a suitable pixel-like representation of the unknown background. Should an anomaly not be present, images of the physical properties are provided. In the case where a anomalies do exist, in addition to the images, we obtain an explicit representation of the shape, location, and contrast of the objects. Thus, the method we propose here simultaneously addresses both the detection and characterization problems.

Second, we develop a new regularization scheme for problems in which there is a mismatch in the sensitivity of the data to the various properties being imaged. As noted above, for the dual energy CT problem, the Compton scatter effects tends to dominate the photoelectric effect. Such challenges however are not limited to CT. For example, when using diffuse optical tomography for medical imaging problems, we have found sensitivity mismatch when attempting to recover multiple chromophore concentration profiles [24]. More generally, the ideas considered here are of potential use to a much broader range of so-called joint inversion problems where a collection of heterogeneous sensors (acoustic, electromagnetic, optical, mechanical, hydrological) are tasked with developing a single "picture" of a given region of space. With each modality sensitive to its own constitutive properties of the medium, the

modeling and regularization ideas considered here represents a step in fusing information in such scenarios. An example for such an inversion scheme arises in the geophysical imaging context [25] where a joint inversion of DC resistivity and seismic refraction is performed to model subsurface profiles where cross product of the gradients of the reconstructed parameters are used to ensure that the profiles provided by the inversion of each parameter are in total agreement.

While the we present here approach is *potentially* of broad use, in this paper the *specific* concern is its application to the dual energy CT for luggage screening problem. Here, we view the work as a contribution to the use of iterative inversion schemes for this class of problems. Like the MAP approach, image formation is cast as the solution to a variational problem comprised of terms reflecting a level of fidelity to the data and prior information. In this context, the model we propose and the structure of the prior information are new to the dual energy CT literature. In a bit more detail, as was the case in [5], we consider here the recovery of the space-varying structure of the photoelectric and Compton scattering parameters.[1] We model these quantities in a hybrid manner as the superposition of a parametrically defined anomaly (should it exists) and a non-parametric background.

The anomaly model is comprised of a geometric component that is common in the two images and contrast parameters that are specific to the photoelectic and Compton images. In this paper, we employ a newly developed parametric level set based representation for the anomalies. Classical level-set methods was developed for modeling propagation of curves by Osher and Sethian [26] and have been widely used in image processing applications [27], [28], [29] as well as for a variety of inverse problems [30], [31], [32], [33], [34]. They provide a topologically flexible shape-based formulation, elegantly representing multiple objects with complicated geometries. The number of unknowns associated with such a model however is equal to the number of pixels in an image. As such they can be difficult to use when solving inverse problems [35]. Recently, level set methods have been defined based on low order basis functions expansions for the level set function [36]. In the context of image segmentation and topology estimation gradient decent-type methods have been developed for determining the unknown expansion coefficients describing the level set function [37], [38], [39], [40], [41]. An alternative parametric level set model specifically adapted to solving inverse problems was considered in [35]. As discussed in [35], this model is especially attractive as there is no need for reinitialization or narrow-banding; all issues frequently encountered with curve evolution methods for inverse problems. It suffices to incorporate a regularization term that penalizes anomalies with large areas. Moreover, because the order of the model is low (on the order of 10's of unknowns) quasi-Newton methods become quite feasible for the estimation of the parameters.

With these advantages, it is this model that forms the basis for the work here. We apply the parametric level set idea to the dual energy CT problem where detection of the size number and location of objects plays a crucial role. As such we we demonstrate empirically that the detection and localization of these objects becomes possible even if the photoelectric image background reconstruction is not very accurate or a FBP based approach would fail to

---

[1]While a basis-material decomposition could be employed, as discussed previously, it is not clear at the present time which materials are most suitable for the screening problem. Moreover, one contribution of the work here is a new approach to stabilize the recovery of the photoelectric coefficient.

provide reasonable results.

In addition to this approach for describing the shapes of the anomalies, the second component of our anomaly model is the contrast of these object in both the Compton and photoelectric images. Here we exploit the fact that, while the nominal background may be quite variable, for applications such as the one motivating this work, one is searching for objects of specific composition. In other words, the physical properties (Compton scattering and photoelectric coefficients) of any anomaly are known at least to within some degree of precision. We interpret this type of information as providing a set of allowable values for the contrast of the object in the photoelectric - Compton coefficient space. By definition then, this set of values *cannot* be assumed by any pixels *not* in the object; i.e., pixels in the background. These two constraints are enforced explicitly in the variational formulation of the image formation problem.

While a parametric model is used to represent the anomaly, given the lack of structure we assume for the background, a pixel-type approach is used to model the nominal spatial structure of the photoelectric and Compton images. As noted previously, the physics of dual energy CT are such that in noisy situations one can recover the Compton image rather well but the photoelectric image tends to be far less accurate [5], [6], [12]. In an attempt to improve this situation, here we take advantage of the fact that the scene being imaged is the same for both parameters. More specifically, because physical objects are represented by discontinuities in the constitutive properties of the medium, one would expect that edges in both images should be highly correlated. Hence, we introduce a correlation based regularization scheme enforcing structural similarity between the gradients of reconstructed images.

The remainder of this paper is organized as follows. In Section II, we provide the polychromatic CT measurement model as well as the representation of total attenuation in terms of photoelectric effect and Compton scatter. In Section III we describe the shape based model via a parametric level set function and formulate the Compton and photoelectric images in terms of homogeneous objects of known properties and unknown background pixels. In Section IV the numerical strategy for the solution is described. We cast the inverse problem in an optimization framework in which the solution is the minimizer of a cost function which consists of a data mismatch term and regularization terms. To solve the optimization problem, an alternating minimization algorithm for the shape and background parameters is applied with Levenberg-Marquardt algorithm employed in each phase. Numerical examples are given are given in Section V. Section VI consists of concluding remarks and thoughts about future goals. Finally in the Appendix, we consider a linearized and simplified version of the background reconstruction problem and derive lower bounds for the mean square errors (MSE) in photoelectric absorption and Compton scatter coefficient estimation. Showing the the bounds are significantly different, we give the reader the intuition about the difficulties that arise in photoelectric absorption coefficient reconstruction and explain the motivation that derived us to use the correlation based regularization.

II. Polychromatic Computerized Tomography Formulation

Typical X-ray sources used in CT applications generate an energy spectra roughly between 20KeV and 140KeV [42]. In this energy range X-ray attenuation is dominated by Compton scatter and photoelectric absorption [6] each

of which can be modeled as a product of an energy and material dependent terms as follows

$$\mu(x, y, E) = c(x, y)f_{KN}(E) + p(x, y)f_p(E) \tag{1}$$

where $\mu(x, y, E)$ is the total attenuation, $c(x, x)$ and $p(x, y)$ are the material dependent Compton scatter and photoelectric absorption coefficients respectively. The quantity f_{KN} is the Klein-Nishina cross section for Compton scattering which is given as:

$$f_{KN}(\alpha) = \frac{1 + \alpha}{\alpha^2} \left[\frac{2(1 + \alpha)}{1 + 2\alpha} - \frac{1}{\alpha} \ln(1 + 2\alpha) \right] \\ + \frac{1}{2\alpha} \ln(1 + 2\alpha) - \frac{1 + 3\alpha}{(1 + 2\alpha)^2} \tag{2}$$

where $\alpha = E/510.95 \text{KeV}$. Lastly, f_p approximates the energy dependency of the Photoelectric absorption and given as

$$f_b = E^{-3}. \tag{3}$$

In polychromatic CT the measured quantities are logarithmic projections obtained at several measurement points defined formally as:

$$P(\phi, x') = -\ln \frac{Y(\phi, x')}{Y_0}. \tag{4}$$

Here $Y(\phi, x')$ is a Poisson random variable with mean

$$\overline{Y}(\phi, x') = \int S(E) \exp\big(-f_{KN}(E) A_c(\phi, x') \\ - f_p(E) A_p(\phi, x')\big) dE + r(\phi, x') \tag{5}$$

where $S(E)$ is X-ray spectrum, ϕ is the measurement angle, x' is tilted version of x axis by ϕ, $r(\phi, x')$ is the background signal caused by scatter and detector noise; $A_c(\phi, x')$ and $A_p(\phi, x')$ are the Radon transforms for the x-ray path (see Fig. 1) of each measurement of Compton scatter and photoelectric absorption coefficients respectively and given as the following:

$$A_c(\phi, x') = \int c(x, y)\delta(x \cos\theta + y \sin\theta - x') dxdy, \tag{6}$$

$$A_p(\phi, x') = \int p(x, y)\delta(x \cos\theta + y \sin\theta - x') dxdy. \tag{7}$$

We call $c(x, y)$ the Compton and $p(x, y)$ the photoelectric images. The blank scan, Y_0, is assumed to be constant for all (ϕ, x') and given as

$$Y_0 = \int S(E) dE. \tag{8}$$

We define the reconstruction domain $\mathcal{D} \subset \mathbb{R}^2$ as a two dimensional rectangular region such that

$$\mathcal{D} = \{(x, y) : 0 \le x \le l_x, 0 \le y \le l_y\}. \tag{9}$$

In order to obtain a discrete representation of (6) and (7) we assume that $c(x, y)$ and $p(x, y)$ are piecewise constant on each pixel of a regular grid with collection of N_p pixels and define the vectors $\mathbf{c} = [c_1, \ldots, c_{N_p}]^T$ and $\mathbf{p} = [p_1, \ldots, p_{N_p}]^T$ to be lexicographically ordered collection of pixels values. Now, (6) and (7) can be rewritten in
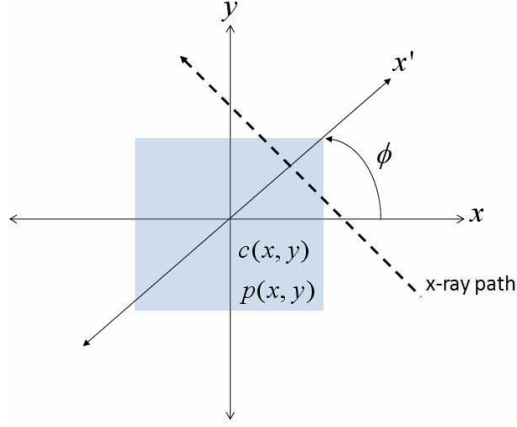
Fig. 1. Geometry of the Radon transform

a matrix form using system matrix $\mathbf{A} = \{a_{ij}\}$ where a_{ij} represents the length of that segment of ray i passing through pixel j.

In this work we assumed parallel beam projections performed for N_θ different angles between 0 and 180 degrees. For each angle, x-ray intensities on equally spaced x' points are recorded to give N_m measurements in total. The measurement is repeated for low and high energy source spectra to constitute the vector $\mathbf{m}^T = [\mathbf{m}_L^T, \mathbf{m}_H^T]$ which consists of $2N_m$ elements. Using the discrete grid and the system matrix $\mathbf{A}$, the ith measurement for low and high energy levels are written as follows:

$$[\mathbf{m}_L]_i = -\ln \frac{[\mathbf{Y}_L]_i}{Y_{0,L}} \tag{10}$$

and

$$[\mathbf{m}_H]_i = -\ln \frac{[\mathbf{Y}_H]_i}{Y_{0,H}}. \tag{11}$$

Similar to the continuous case $\mathbf{Y}_L$ and $\mathbf{Y}_H$ are vectors of Poisson random variables with means

$$[\overline{\mathbf{Y}}_L]_i = \int S_L(E)\exp\big(-f_{KN}(E)\mathbf{A}_{i*}\mathbf{c} \\ - f_p(E)\mathbf{A}_{i*}\mathbf{p}\big)\mathrm{d}E + r_{L,i} \tag{12}$$

and

$$[\overline{\mathbf{Y}}_H]_i = \int S_H(E)\exp\big(-f_{KN}(E)\mathbf{A}_{i*}\mathbf{c} \\ - f_p(E)\mathbf{A}_{i*}\mathbf{p}\big)\mathrm{d}E + r_{H,i} \tag{13}$$

where $\mathbf{A}_{i*}$ is the ith row of $\mathbf{A}$, $S_L(E)$ and $S_H(E)$, corresponds to low energy and high energy X-ray spectra which are shown in Fig. 2. In our work, these spectra with 1 keV energy bins were obtained using *SpekCalc*, a free of charge software program which calculates x-ray spectra from tungsten anode tubes where specifications such as tube voltage and filtration thickness are assigned via a friendly user interface [43], [44], [45]. Distinct energy levels are obtained by alternating the tube voltage between 80 keV and 140 keV. The total number of photons for $S_L(E)$
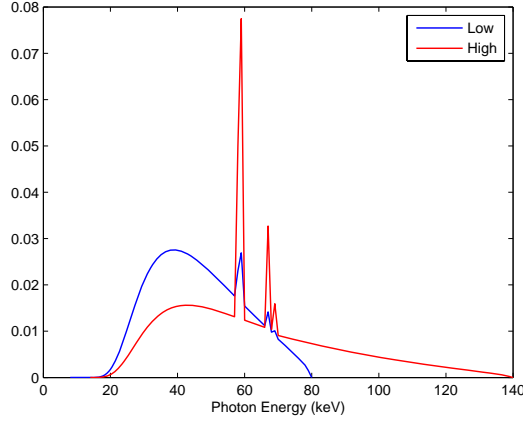
Fig. 2.   Normalized X-ray Energy Spectra

is 1.8×10^6 and for $S_H(E)$ is 3.6×10^6. The combination of scatter and detector readout noise contributions are denoted by $r_{L,i}$ and $r_{H,i}$. In practice these contributions are not known *a priori* since they are related to object properties (shape and chemical composition) and scanner specification. However, scatter is a smoothly varying signal which can be estimated [46], [47] and often assumed known [46] or characterized by constant primary-to-scatter ratio [48], [49]. On the other hand, detector readout noise characteristics can be approximated by a Gaussion distribution [50]. Here, we assume $r_{L,i}$ and $r_{H,i}$ are additive white Gaussian (AWGN) and call them background noise. For a more advanced treatment of scatter see [51].

III. THE PARAMETRIC LEVEL-SET MODEL AND REPRESENTATION OF COMPTON AND PHOTOELECTRIC IMAGES

Compton scatter and photoelectric absorption coefficients are the main interests of our polychromatic CT problem and can be regarded as two different images to be reconstructed. Each image is assumed to be formed by piecewise constant objects of interest on an unknown background. For a domain $\Omega \subset \mathcal{D}$ which represents the support of the objects of interest, the characteristic function $\chi(x, y)$ is defined as

$$\chi(x, y) = \begin{cases} 1, & \text{if}(x, y) \in \Omega \\ 0, & \text{if}(x, y) \in \mathcal{D} \backslash \Omega. \end{cases} \tag{14}$$

Now, the Compton and photoelectric images can be written as

$$c(x, y) = \chi(x, y)c_a + [1 - \chi(x, y)]\, c_b(x, y) \tag{15}$$

and

$$p(x, y) = \chi(x, y)p_a + [1 - \chi(x, y)]\, p_b(x, y). \tag{16}$$

Here c_a and p_a are Compton scatter and photoelectric absorption coefficients of the anomaly (object of interest) and assumed to be constant; whereas $c_b(x, y)$ and $p_b(x, y)$ are low order basis expansion representation of the

background images given as

$$c_b(x,y) = \sum_{i=1}^{N_b} \beta_i B_i(x,y) \tag{17}$$

and

$$p_b(x,y) = \sum_{i=1}^{N_b} \alpha_i B_i(x,y) \tag{18}$$

where $\{\beta_i\}$ and $\{\alpha_i\}$, $i = 1, \ldots, N_b$ are the sets of Compton and photoelectric expansion coefficients to be determined and $\{B_i(x,y)\}$ is the set of predefined basis functions. The order of the expansion, N_b, is determined depending on the desired resolution. Pixels or smoother alternatives as radial basis functions can be chosen depending on the desired resolution. This approach provides us with the possibility to reduce the number of unknowns significantly and is well suited for applications where a coarser representation of the background is acceptable. Low order basis expansion formula proved to be successful for monoenergetic x-ray tomography [33], [37].

The characteristic function $\chi(x,y)$ is defined to be the zero level set of an Lipschitz continuous object function $\mathcal{O} : \mathcal{D} \longrightarrow \mathbb{R}$ such that $\mathcal{O}(x,y) > 0$ in Ω, $\mathcal{O}(x,y) < 0$ in $\Omega \backslash \mathcal{D}$ and $\mathcal{O}(x,y) = 0$ in $\partial\Omega$. Using $\mathcal{O}(x,y)$, $\chi(x,y)$ is written as

$$\chi(x,y) = H(\mathcal{O}(x,y)) \tag{19}$$

where H is the step function. In practice, H_ϵ and its derivative δ_ϵ which are smooth approximations of the step function and Dirac delta function respectively, are used [52]. For $\epsilon \in \mathbb{R}^+$ we have the following:

$$H_\epsilon(x) = \begin{cases} \frac{1}{2}\left(1 + \frac{2}{\epsilon} + \frac{1}{\pi} sin\left(\frac{\pi x}{\epsilon}\right)\right) & \text{if } |x| \leq \epsilon \\ 1 & \text{if } x > \epsilon \\ 0 & \text{if } x < -\epsilon \end{cases} \tag{20}$$

and

$$\delta_\epsilon(x) = \begin{cases} \frac{1}{2\epsilon}\left(1 + sin\left(\frac{\pi x}{\epsilon}\right)\right) & \text{if } |x| \leq \epsilon \\ 0 & \text{otherwise.} \end{cases} \tag{21}$$

This kind of implicit (i.e. level set) representation of regions is a well-known approach successfully applied to image processing [27] as well as image formation problems [53]. The object function $\mathcal{O}(x,y)$, is represented parametrically using a predefined basis set as

$$\mathcal{O}(x,y) = \sum_{i=1}^{L} a_i p_i(x,y) \tag{22}$$

where a_i's are the weight coefficients whereas $p_i(x,y)$ are the functions which belong to the basis set of $\mathcal{P} = \{p_1, p_2, \ldots, p_L\}$. The shape estimation problem then is reduced to the determination of a set of expansion coefficients using a quasi-Newton method (see Section 5). Consequently, we eliminate the requirement of a reinitialization process as well as implementation of narrow band methods which are essential for the standard approach where a signed distance function is used for the level set function and a curve evolution is performed. Additionally, well known properties of the level set approach of such as topological flexibility and capability to represent multiple objects is maintained [52].

In this work, we used exponential radial basis functions (RBF's) for the background basis set $\{B_i(x,y)|i = 1, \ldots, N_b\}$ and object function basis set $\{p_i(x,y)|i = 1, \ldots, L\}$. Exponential RBFs are defined as

$$\Phi_i(\mathbf{r}) = \exp\left(-\frac{\|\mathbf{r} - \mathbf{r}_i\|^2}{\sigma^2}\right). \tag{23}$$

Here $\Phi_i : \mathcal{R}^2 \to \mathcal{R}$ is the i$^{\text{th}}$ RBF, $\mathbf{r} = (x,y)$ is the Cartesian coordinates vector, $\mathbf{r_i}$ is the center of i$^{\text{th}}$ basis function and σ is the width which is fixed for all RBFs in the basis set. Once the number of elements in the basis set is determined σ's can be determined by a least squares fit to simple geometries [54].

Let us gather all the parameters of our model in vector $\boldsymbol{\theta}^T = \left[c_a, p_a, \mathbf{a}^T, \boldsymbol{\beta}^T, \boldsymbol{\alpha}^T\right]$ where $\boldsymbol{a} = [a_1, \ldots, a_L]^T$, $\boldsymbol{\alpha} = [\alpha_1, \ldots, \alpha_{N_b}]^T$, and $\boldsymbol{\beta} = [\beta_1, \ldots, \beta_{N_b}]^T$. Now, for the set of model parameters $\boldsymbol{\theta}$, the high and low energy projection models given in (10) and (11) can be expressed in a operator form: $K(\boldsymbol{\theta}) = \left[K(\boldsymbol{\theta})_L^T, K(\boldsymbol{\theta})_H^T\right]^T$. We define the matrix $\mathbf{B} \in \mathcal{R}^{N_p \times N_b}$ as the discretized basis matrix where $[\mathbf{B}]_{ij}$ is the value of $B_j(x,y)$ at the center of ith pixel. Now, the vector of Compton background and photoelectric background images can be expressed as $\mathbf{B}\boldsymbol{\beta}$ and $\mathbf{B}\boldsymbol{\alpha}$ respectively. Finally, we denote the lexicographical order of discretized object function $\mathcal{O}(x,y)$ with the vector $\mathcal{O} \in \mathcal{R}^{N_p}$.
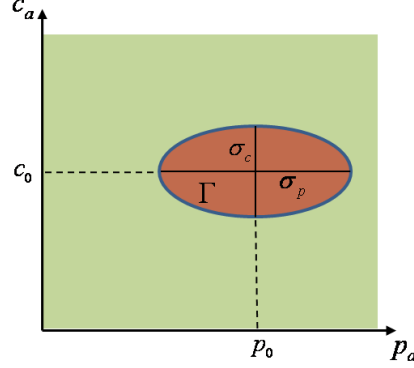
IV. RECONSTRUCTION ALGORITHM

In our variational framework, we seek for an estimate $\hat{\boldsymbol{\theta}}$ of the unknown parameter vector $\boldsymbol{\theta}$ minimizing an objective functional $F(\boldsymbol{\theta})$ which is composed of a data misfit term and regularization terms which incorporate prior information, subject to a set of non-linear constraints as

$$
\begin{aligned}
\text{minimize} \quad & F(\boldsymbol{\theta}, \boldsymbol{\lambda}) = \frac{1}{2}\left(K(\boldsymbol{\theta}) - \mathbf{m}\right)^T \boldsymbol{\Sigma}\left(K(\boldsymbol{\theta}) - \mathbf{m}\right) \\
& \qquad\qquad + R(\boldsymbol{\theta}, \boldsymbol{\lambda}) \\
\text{subject to} \quad & (p_a, c_a) \in \Gamma \\
& ([\mathbf{B}\boldsymbol{\beta}]_i, [\mathbf{B}\boldsymbol{\alpha}]_i) \notin \Gamma, \quad \text{for} \quad i = 1, \ldots, N_p.
\end{aligned}
\tag{24}
$$

Here the constraints account for our prior knowledge about the physical properties of the objects. We interpret this type of prior information as providing a subset Γ of allowable values for the contrast of the object in the $c_a - p_a$ parameter space which also corresponds to pairs of values that cannot be found in the reconstruction of the background. While in general the set of allowable parameter values could be comprised of a number of disconnected regions (as would be the case where there were a number of possible chemical compounds of interest each characterized by its own uncertainty set), for simplicity here we consider the case where the constraint set is elliptical in shape. We define $\Gamma \in \mathcal{R}^2$ as an ellipse with the center (c_0, p_0) major axis σ_p and minor axis σ_c (see Fig. 3 for a symbolic representation). Now, we can write two sets of non-linear inequality constraints $g_1(p_a, c_a) : \mathcal{R}^2 \to \mathcal{R}$ and $\boldsymbol{g}_2(\boldsymbol{\beta}, \boldsymbol{\alpha}) : \mathcal{R}^{2N_b} \to \mathcal{R}^{N_p}$ regarding the object and background contrast values respectively as

$$g_1(p_a, c_a) = \frac{(c_a - c_0)^2}{\sigma_c^2} + \frac{(p_a - p_0)^2}{\sigma_p^2} - 1 \tag{25}$$

Fig. 3. Region Γ for object of interest parameters

and

$$\boldsymbol{g}_{2,i}(\boldsymbol{\beta}, \boldsymbol{\alpha}) = -\frac{([\mathbf{B}\boldsymbol{\beta}]_i - c_0)^2}{\sigma_c^2} - \frac{([\mathbf{B}\boldsymbol{\alpha}]_i - p_0)^2}{\sigma_p^2} + 1$$

$$, \text{for} \quad i = 1, \ldots, N_p.$$

(26)

The optimization problem with these inequality constraints can be rewritten as

$$\text{minimize} \quad F(\boldsymbol{\theta}, \boldsymbol{\lambda}) = \frac{1}{2}\big(K(\boldsymbol{\theta}) - \mathbf{m}\big)^T \boldsymbol{\Sigma}\big(K(\boldsymbol{\theta}) - \mathbf{m}\big)$$

$$+ R(\boldsymbol{\theta}, \boldsymbol{\lambda})$$

$$\text{subject to} \quad g_1(p_a, c_a) \leq 0,$$

$$\boldsymbol{g}_2(\boldsymbol{\beta}, \boldsymbol{\alpha}) \leq 0.$$

(27)

X-ray interactions, hence the photon count at the detector, is governed by a Poisson process [42]. Statistical inversion algorithms, where the exact log-likelihood of Poisson distribution is used, have been successfully applied to medical imaging problems [20], [16], [46]. Sauer and Bouman [55] derived the weighted least squares data misfit term given in (24) and (27) as a quadratic approximation of the Poisson log likelihood function which is successfully applied to dual energy CT problem [14]. In their approach the error terms are weighted by the number of counts at the detector such that $\boldsymbol{\Sigma} = \text{diag}(\mathbf{m})$. In transmission tomography measurements with low intensities (low photon counts) correspond to rays coincide with highly attenuating objects and have low SNR. Therefore, the measurements with high intensities are considered to be more reliable and highly weighted. From a different point of view, if the photon count is large as will be the case here, the Poisson distribution can be approximated by a Gaussian distribution [50], [56]. Furthermore, energy integrating detectors used in commercial CT scanners cause the statistics to deviate from Poisson distribution [57] and their noise characteristics are well approximated by a Gaussian distribution [14], [58]. In that case one can assume that the total measurement noise is additive Gaussian with zero mean and invertible covariance matrix Γ_{noise} and set $\boldsymbol{\Sigma}$ equal to $\Gamma_{\text{noise}}^{-1}$. In this work we assume that each measurement is independent and of equal quality; hence set $\boldsymbol{\Sigma} = \sigma\mathbf{I}$. This approach had been successfully applied to limited data CT [59] application and we feel it is reasonable for this work since artifacts which are
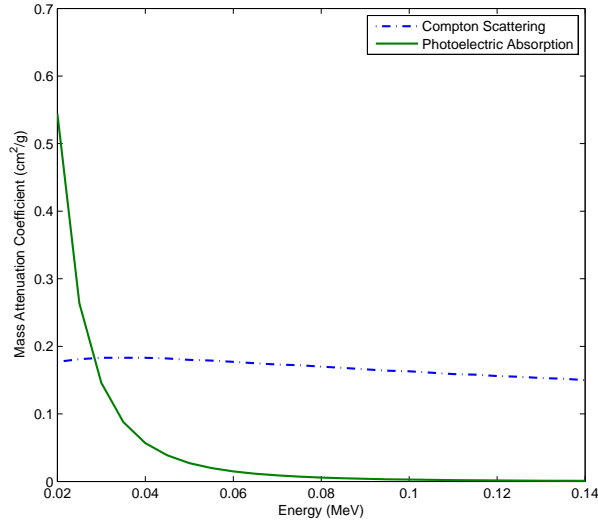
Fig. 4.   Comparison of mass attenuation coefficients due to Compton scatter and photo electric effect for water.

caused by high density materials are complications that we prefer to consider at a later time (See Section VI).

The regularizer $R(\boldsymbol{\theta})$ has two terms which penalizes over-sized objects of interest and allows for the use of photoelectric absorption-Compton Scatter basis model.

$$R(\boldsymbol{\theta}, \boldsymbol{\lambda}) = R_1(\boldsymbol{a}) + R_2(\boldsymbol{\alpha}, \boldsymbol{\beta}). \tag{28}$$

First is the commonly used penalty term [27], [31] that encourages objects of interest to have a small area:

$$R_1(\boldsymbol{a}) = \lambda_1 \|H(\boldsymbol{\mathcal{O}})\|_1. \tag{29}$$

As stated in (1) and (3), due to the E^{-3} energy dependency of photoelectric absorption, especially for photon energies greater than 50 KeV, the contribution of the photoelectric absorption to the total attenuation is very small compared to that of Compton scatter [48]. Fig. 4 demonstrates a comparison of the contributions of both phenomenon to the total x-ray attenuation for water as a function of energy. The cross section data for this figure is taken from Xcom: Photon cross section database [60]. For instance at 80 KeV Compton scatter cross section is $1.7 \times 10^{-1} \mathrm{cm}^2/\mathrm{g}$ whereas photoelectric absorption cross section is $5.77 \times 10^{-3} \mathrm{cm}^2/\mathrm{g}$ (i.e. roughly 30 times smaller). Hence, there is severe mismatch between sensitivities of the measurement model to these components. Therefore, for noisy data, reconstruction of the photoelectric component requires additional effort especially as the total attenuation of the scene increases. In the Appendix, we perform a sensitivity analysis of linearized version of the background reconstruction problem and show that the lower bound of the error in the estimation of photoelectric absorption coefficient is significantly larger than that of the Compton scatter coefficient. One way to ameliorate such a situation is to introduce an appropriate regularization scheme. As we are reconstructing two different parameters (Compton scatter and photoelectric absorption coefficients) of the same object, one would expect spatial co-variation

between reconstructed images of these parameters. That is to say orientation of the boundaries should be similar although intensity variations within individual images may differ. We exploit this *a priori* information by enforcing similarity between gradient vectors of the images of these parameters. This kind of approach was previously used in the context of geophysical imaging where Gallardo *et al.* performed a joint inversion of DC resistivity and seismic refraction to characterize 2D subsurface profiles [25], [61]. Their approach to enforcing structural similarity via a constraint in the optimization process required that the cross product of the gradient vectors associated with the two properties should vanish.

In our case, however, we seek structural co-variation (i.e., two images should be similar in some sense but might not be identical) between reconstructed images. Our aim is to incorporate this *a priori* information to regularize our problem in a variational sense rather than imposing a constraint on the optimization process. As the boundary of the object of interest is identical in both images (i.e., $\chi(x, y)$) it suffices to deal only with background images. Herein we introduce the following correlation type of metric

$$R_2(\boldsymbol{\alpha}, \boldsymbol{\beta}) = \lambda_2 \left[\frac{\|\mathbf{DB}\boldsymbol{\beta}\|_2^2 \|\mathbf{DB}\boldsymbol{\alpha}\|_2^2}{\left[(\mathbf{DB}\boldsymbol{\beta})^T (\mathbf{DB}\boldsymbol{\alpha}) \right]^2} - 1 \right]^2 \tag{30}$$

where $\mathbf{D}$ is the gradient matrix defined as $\mathbf{D} = [\mathbf{D}_x \ \mathbf{D}_y]$ with the first difference matrices $\mathbf{D}_x$ and $\mathbf{D}_y$ in x and y direction respectively. It is easily seen that F_2 decreases as the correlation of the gradients increase in negative or positive direction and vanishes when they are perfectly correlated or anti-correlated.

The constants $\{\lambda_i\}_{i=1,2}$ associated with each term in $R((\theta)$ tunes the trade off between the fidelity of the solution to the observed data, incorporation of *a priori* information and regularization. Optimal choice of multiple regularization parameters is a challenging problem. L-curve [62], generalized cross validation(GCV) [63] and discrepancy principle [64] are the most frequently used methods for optimal choice of multiple regularization parameters. Although systematic selection of parameters is provided with these methods, the problem is not straightforward and requires running the optimization code several times. In this work, we tuned the regularization parameters λ_1 and λ_2 by hand such that the values that give the best results judged by the eye were assigned. Empirically speaking, for values bigger then an optimum value of λ_2, reconstruction quality remains the same while number iterations to obtain that quality increases, therefore the process becomes more time consuming.

The solution to (27) is obtained using an exact penalty approach where the constrained problem is transformed to an unconstrained one so that the transformed cost functional has the same minima as the original one. This is achieved by adding a term penalizing infeasible regions to the objective functional, then performing minimization using an appropriate unconstrained optimization technique [65]. Specifically, in this work we used the following penalty function

$$P(r, c_a, p_a, \boldsymbol{\beta}, \boldsymbol{\alpha}) = r \left(g_1^+(c_a, p_a) + \sum_{i=1}^{N_p} \boldsymbol{g}_{2,i}^+(\boldsymbol{\beta}, \boldsymbol{\alpha}) \right) \tag{31}$$

where $f^+(x) = \max(f(x), 0)$ and r is the penalty parameter. As differentiability of the penalty term will be required

we use the following smooth approximation [66] of $\max(x, 0)$ function:

$$\max(x, 0) \approx \frac{1}{2}(\sqrt{x^2 + \epsilon} + x) \tag{32}$$

where $\epsilon \in \mathcal{R}^+$ is small.

According to exact penalty theorem [65] If $\boldsymbol{\mu}$ are the Lagrange multipliers of the original problem, for $r > \max(\mu_i : i = 1, \ldots, 1 + N_p)$ the local minima of (27) is also the local minima of the following unconstrained problem:

$$F_p(\boldsymbol{\theta}, \boldsymbol{\lambda}, r) = \frac{1}{2}\big(K(\boldsymbol{\theta}) - \mathbf{m}\big)^T \boldsymbol{\Sigma}\big(K(\boldsymbol{\theta}) - \mathbf{m}\big)$$
$$+ R(\boldsymbol{\theta}) + P(r, c_a, p_a, \boldsymbol{\beta}, \boldsymbol{\alpha}). \tag{33}$$

As opposed to other methods to solve constraint optimization problems such as quadratic penalty method where one needs to solve sequence of sub-problems with increasing penalty parameter, it suffices to find one r that will be fixed during the minimization process. Finding the Lagrange multipliers, however, is a hard problem. Nonetheless, the value of the penalty parameter r can be determined relatively easier than λ_i's as the solution is not prone to fail with changes in r and it suffices to, heuristically, set it large enough so that the constraints are satisfied [66]. We found this approach satisfactory for the purpose and the minimization algorithm (Levenberg-Marquardt) of this work. For an adaptive penalty parameter update strategy for a Sl_1QP [67] based method, we refer the reader to the work of Byrd $et\ al.$ [68].

The minimization of the cost function in (33) is achieved by Levenberg-Marquardt algorithm [69]. For this aim the cost function is rewritten in terms of an error vector ϵ as

$$F_p(\theta) = \boldsymbol{\epsilon}(\boldsymbol{\theta})^T \boldsymbol{\epsilon}(\boldsymbol{\theta}). \tag{34}$$

The error term has the form $\boldsymbol{\epsilon}(\boldsymbol{\theta})^T = \left[\epsilon_1^T, \epsilon_2^T, \epsilon_3, \epsilon_4^T\right]$ where each term is associated with the corresponding term in the cost functional and given as

$$\epsilon_1 = K(\boldsymbol{\theta}) - \mathbf{m}, \tag{35}$$

$$\epsilon_2(\mathbf{a}) = \sqrt{\lambda_1 H(\mathcal{O})}, \tag{36}$$

$$\epsilon_3(\boldsymbol{\alpha}, \boldsymbol{\beta}) = \sqrt{\lambda_2}\left(\frac{\|D\boldsymbol{\beta}\|_2^2\|D\boldsymbol{\alpha}\|_2^2}{(D\boldsymbol{\beta})^T(D\boldsymbol{\alpha})} - 1\right) \tag{37}$$

and

$$\epsilon_4 = \sqrt{r}\left[\sqrt{g_1^+(c_a, p_a)}, \sqrt{g_{2,1}^+(\boldsymbol{\alpha}, \boldsymbol{\beta})}, \ldots, \sqrt{g_{2,N^p}^+(\boldsymbol{\alpha}, \boldsymbol{\beta})}\right]^T. \tag{38}$$

In order to employ Levenberg-Marquardt algorithm, calculation of the Jacobian matrix J, whose rows are the derivatives of $\boldsymbol{\epsilon}(\boldsymbol{\theta})$ with respect to each element in the unknown parameter vector $\boldsymbol{\theta}$, is required. In detail, nth column of J is the derivative of $\boldsymbol{\epsilon}(\boldsymbol{\theta})$ with respect to nth element in the parameter vector $\boldsymbol{\theta}$.

$$\mathbf{J} = \left[\frac{\partial \boldsymbol{\epsilon}(\boldsymbol{\theta})}{\partial \{c_a, p_a, \mathbf{a}, \boldsymbol{\beta}, \boldsymbol{\alpha}\}}\right]. \tag{39}$$

These derivatives are easily obtained analytically. The details are omitted here, although the Appendix provides some intuition. The solution is obtained by updating $\boldsymbol{\theta}$ each iteration as the following

$$\boldsymbol{\theta}^{n+1} = \boldsymbol{\theta}^n + \mathbf{h} \tag{40}$$

where h is the solution of the following linear system at each iteration

$$(\mathbf{J}^T\mathbf{J} + \mu\mathbf{I})\mathbf{h} = -\mathbf{J}^T\boldsymbol{\epsilon} \;\; \text{with} \;\; \mu \geq 0. \tag{41}$$

Here $\mathbf{I}$ is the identity matrix, μ is the damping parameter affecting the size and direction of $\mathbf{h}$ and it is adaptively tuned during the iteration process [70].

V. NUMERICAL EXAMPLES

To validate our method we performed reconstructions from simulated data according to the data acquisition models given in (10) and (11). The background signals $\mathbf{r}_L$ and $\mathbf{r}_H$ are simulated as white Gaussian noise. Parallel beam measurements are simulated for equally spaced 30 angles between 0 and 180 degrees each with 150 source-detector pairs. We compare our results with the method proposed in [5] which is based on estimation of two sinograms corresponding to Compton scatter and photoelectric absorption then using a FBP method to reconstruct the final images. Their work is also based on reconstructing Compton scatter and photoelectric absorption properties with a FBP approach; therefore it gives us the opportunity to compare the performance of our method with the standard method that is proposed for luggage screening purposes. A Ram-Lak filter multiplied with a Hamming window was used in the FBP inversion. We will call this method DEFBP (dual energy FBP). We also applied thresholds to the reconstructed images to reveal regions $\boldsymbol{\chi}_t$ of object of interest defined by the region Γ (see Fig. 3). Specifically if reconstructed Compton and photoelectric images are $\mathbf{I}_c$ and $\mathbf{I}_p$ respectively then $\boldsymbol{\chi}_t$ can be calculated with the Hadamard product as

$$\boldsymbol{\chi}_t = \boldsymbol{\chi}_\mathbf{c} \circ \boldsymbol{\chi}_\mathbf{p} \tag{42}$$

where $\boldsymbol{\chi}_\mathbf{c}$ and $\boldsymbol{\chi}_\mathbf{p}$ are given as

$$[\boldsymbol{\chi}_{\mathbf{c(p)}}]_{ij} = \begin{cases} 1 & \text{if } \left| [\boldsymbol{\chi}_{\mathbf{c(p)}}]_{ij} - c(p)_0 \right| \leq \sigma_{c(p)} \\ 0 & \text{otherwise.} \end{cases} \tag{43}$$

In the minimization process we followed a coordinate decent type algorithm where object boundary(shape) parameters ($\{a_i\}$) are updated while contrast parameters are kept fixed and then contrast parameters ($\boldsymbol{\beta}$, $\boldsymbol{\alpha}$, c_a, p_a) are updated while level set parameters are fixed. Convergence is checked for each individual cycle using the stopping condition [70]

$$\|\mathbf{x}^k - \mathbf{x}^{k-1}\| < \epsilon(1 + \|\mathbf{x}^{k-1}\|) \;\; \text{or} \;\; k > k_{\max} \tag{44}$$

where $\mathbf{x}^k$ corresponds to vector of shape or contrast parameters at k^{th} iteration, $k_{\max}$ is maximum number of iterations and ϵ is a small, positive number which is taken 10^{-6}. Once both cycles are completed the overall convergence is checked using the same criteria given in (44) on the reconstructed photoelectric and Compton image vectors.
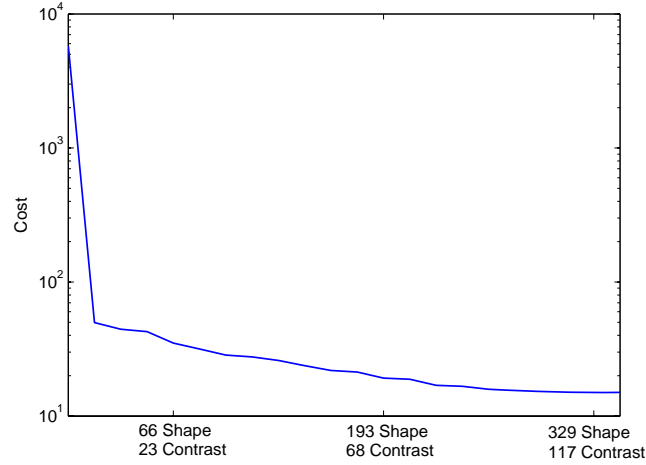
Fig. 5.   The value of the cost function F, versus number of iterations for the example shown in Fig. 6.

Quantitative accuracy of reconstructions are determined by relative L^2-error which is given as

$$E_{L^2} = \frac{\parallel \hat{\mathbf{I}} - \mathbf{I} \parallel_2^2}{\parallel \mathbf{I} \parallel_2^2}. \tag{45}$$

Here, $\hat{\mathbf{I}}$ is the reconstruction of either the Compton image or the photoelectric image and $\mathbf{I}$ is the corresponding true image. The accuracy of the boundary reconstruction $\hat{\chi}$ compared to the true boundary χ is determined using the Dice's coefficient. Assuming $\hat{\chi}$ and χ are sets of points in space where the points are corresponding pixels of the object of interest, Dice's coefficient is given as

$$D_{\chi} = \frac{2|\hat{\chi} \cap \chi|}{|\hat{\chi}| + |\chi|}. \tag{46}$$

Here $D_{\chi} = 1$ shows maximum similarity (i.e., the sets are identical) and $D_{\chi} = 0$ shows the sets do not have a common point (i.e., the sets are disjoint).

For all examples, $N_b = 676$ RBF's with $\sigma_b = 6\Delta x$ where Δx is the length of one pixel were used for background representation given in (17) and (18). This corresponds to a RBF for every 4x4 super-pixel and 676 unknown coefficients for each background image instead of 10^4 which would have been the case for a pixel based reconstruction. For the level set function we used $L = 144$ RBF's with $\sigma_s = 10\Delta x$ as the basis set. The level set function is initialized randomly whereas background parameters $\boldsymbol{\beta}$ and $\boldsymbol{\alpha}$ are set to 8×10^{-3} and 80 respectively. These values are chosen so that the contrast of initial background images were small. The regularization parameters, λ_1 and λ_2 were set to 0.1 and 10 respectively; whereas the penalty parameter, r was set to 10^5.

The first set of phantoms that consist of objects with various shapes and constant intensities on a homogeneous background have the size of 20x20 cm and discretized into 100×100 pixels. We emphasize that the geometry of the photoelectric absorption and Compton scatter phantoms are taken to be same although the contrasts are different as the images represent distinct physical properties of the medium. The object of interest parameters that define Γ are set as the following: $c_0 = 0.19$, $\sigma_c = 0.05$, $p_0 = 5000$, $\sigma_p = 500$; and the boomerang shaped object on lower left is assigned as an object of interest (see first row of Fig. 6) with $c_a = 0.2$ and $p_a = 5000$. These parameters
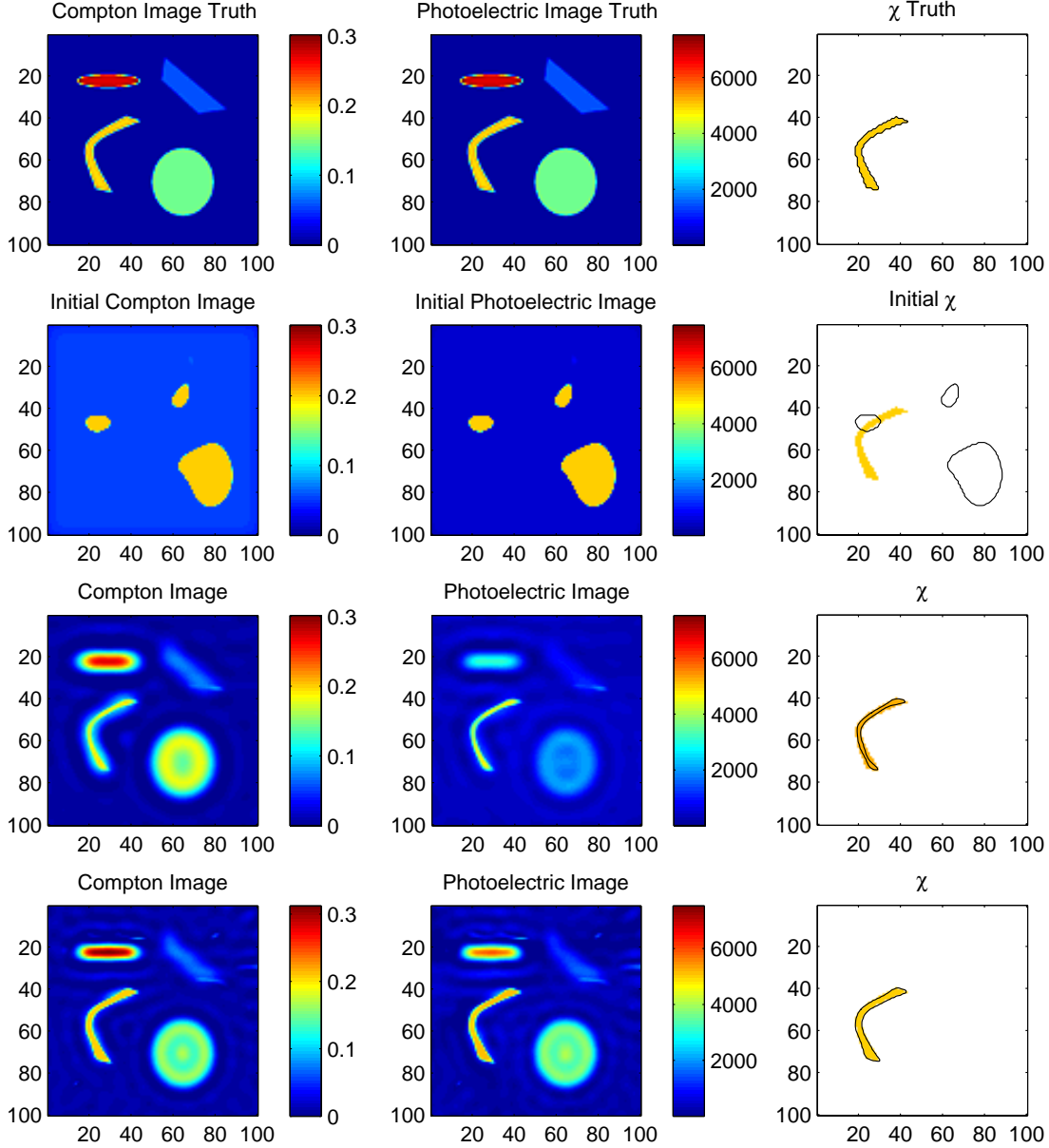
Fig. 6.   Simulation with the first phantom with 60dB background noise. First row: Ground truth images. Second row: initial images. Third row: Reconstruction after 3 cycles of shape and contrast updates. Fourth row: Final reconstructions after 11 cycles. First column: Compton image. Second column: Photoelectric image. Third column: Characteristic function, χ, of the object. The solid yellow is the true object while the thin line represents the estimated boundary.

are in the range that correspond to real materials that may be present in a luggage and are chosen generically to test our algorithm on objects with moderate attenuation properties.

In the first example the first phantom was used and dual enery measurements are simulated for 60dB background noise. Fig. 5 shows the value of the cost function $F_p(\boldsymbol{\theta}, \boldsymbol{\lambda}, r)$ during minimization process. Fig. 6 shows the actual phantoms for Compton and photoelectric images, initializations for both images as well as the object boundary,
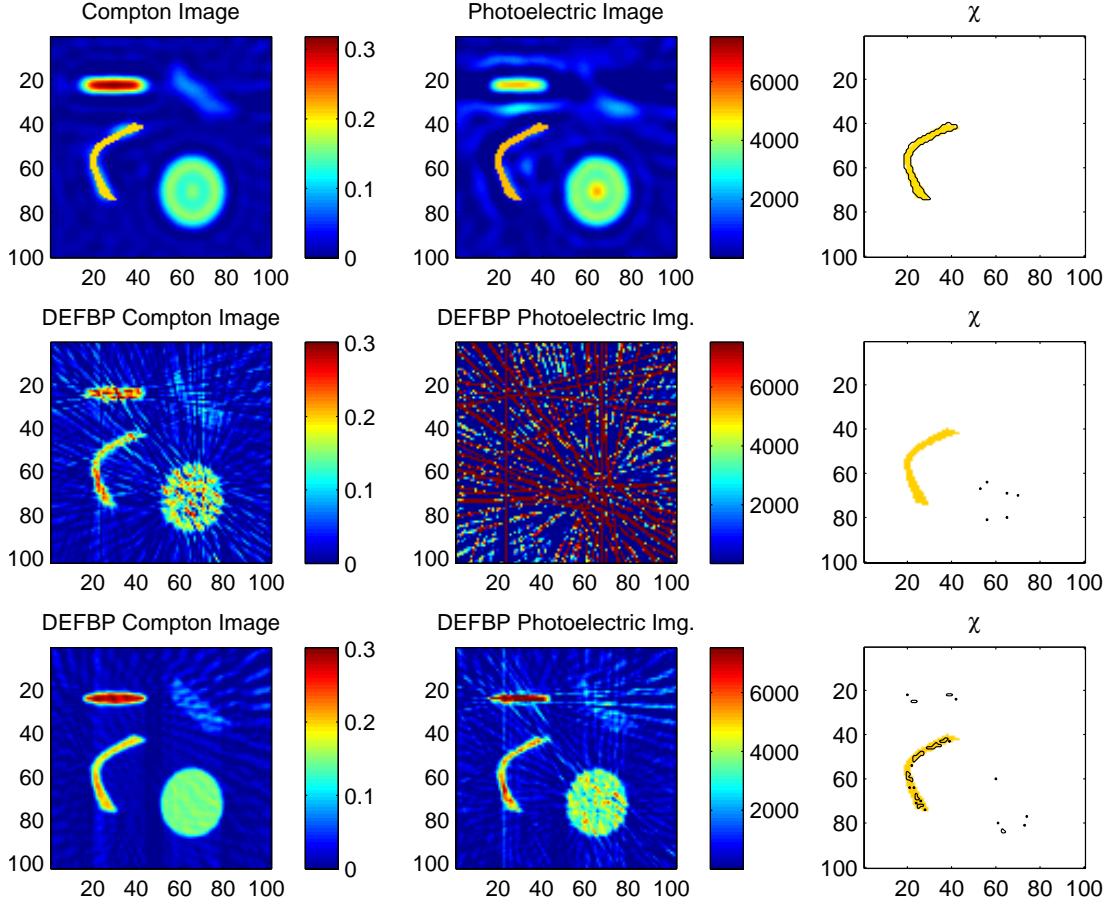
Fig. 7.   Simulation with the first phantom with 60dB background noise. First row: Proposed method without regularizer, R_2. Second row: DEFPB reconstruction. Third Row: DEFBP reconstruction without background noise. First column: Compton image. Second column: Photoelectric image. Third column: Characteristic function, χ, of the object. The solid yellow is the true object while the thin line represents the estimated boundary.

TABLE I

ERROR ANALYSIS FOR THE SIMULATION USING THE FIRST PHANTOM WITH 60DB BACKGROUND NOISE

Method	E_{L^2} Compton	E_{L^2} photoelectric	D_{χ}
Proposed method	0.0741	0.0873	0.9387
Proposed method without R_2	0.0818	0.1977	0.9283
DEFBP	0.4166	129.57	0
DEFBP without b.ground noise.	0.1025	0.3011	0.4229

reconstructions after 3 cycles of shape and contrast updates and the end results after 11 cycles. In the rightmost column, the object boundaries are shown with black solid lines where the yellow object shows the support of the true object of interest. Fig. 7 shows the reconstruction using the proposed method without using the correlation based regularizer R_2 and DEFB reconstructions with 60dB background noise and without background noise.   As
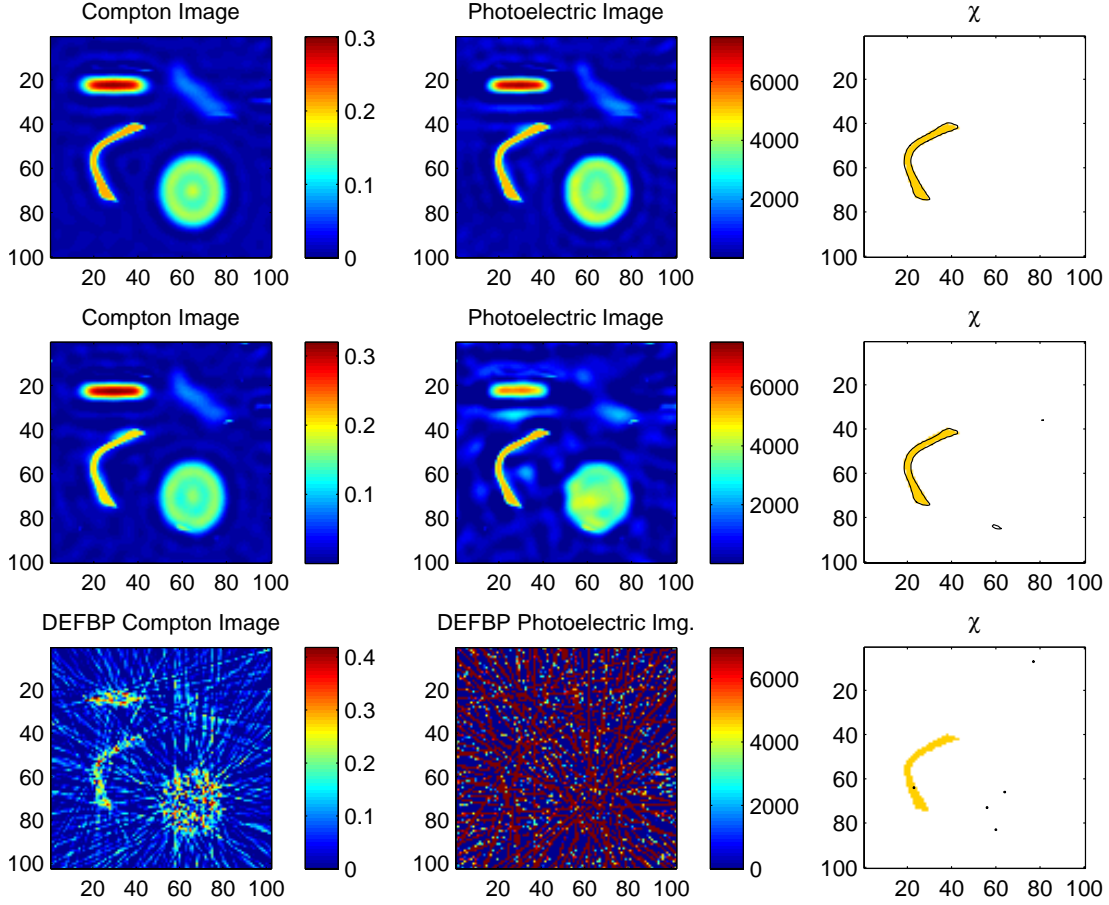
Fig. 8.   Simulation with the first phantom with 40dB background noise. First row: Proposed method. Second row: Proposed method without regularizer, R_2. Third row: DEFPB reconstruction. First column: Compton image. Second column: Photoelectric image. Third column: Characteristic function, χ, of the object. The solid yellow is the true object while the thin line represents the estimated boundary.

TABLE II

ERROR ANALYSIS FOR THE SIMULATION USING THE FIRST PHANTOM WITH 40DB BACKGROUND NOISE

Method	E_{L^2} Compton	E_{L^2} photoelectric	D_χ
Proposed method	0.0908	0.1014	0.9455
Proposed method without R_2	0.0818	0.1886	0.9113
DEFBP	1.7684	293.6438	0.0118

observed from Fig. 6 and Fig. 7 our method provides an accurate reconstruction of the boundaries of the object of interest as well as a reasonable reconstruction of the background images where different objects are clearly visible. On the other hand, DEFBP method provides reasonable reconstructions only in the absence of background noise especially for photoelectric image. It is also observed that using the correlation regularization significantly reduces error in the photoelectric image reconstruction. Quantitative evaluation of the reconstructions in the first example
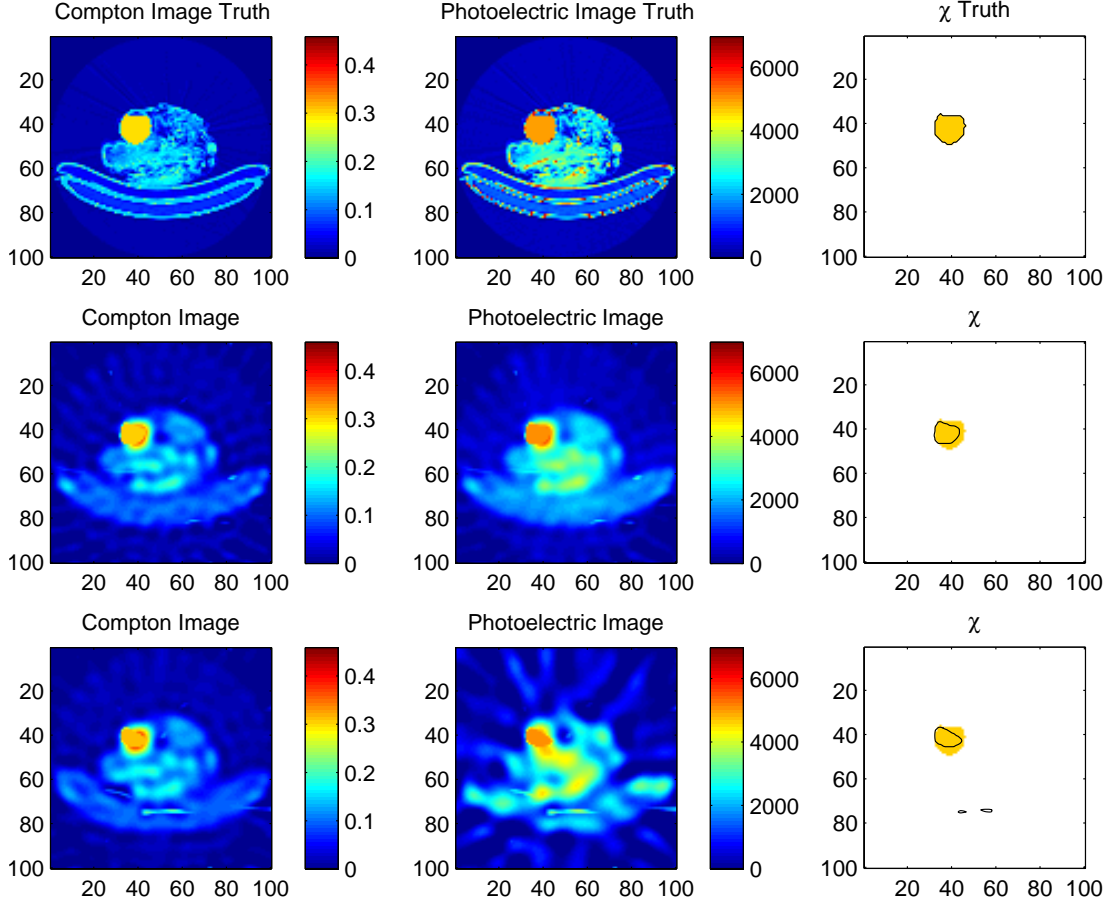
Fig. 9.   Simulation with the duffle bag phantom with 40dB background noise. First row: Ground truth images. Second row: Proposed method. Third row: Proposed method without regularizer, R_2. Third Row: Proposed method without regularizer, R_2. First column: Compton image. Second column: Photoelectric image. Third column: Characteristic function, χ, of the object. The solid yellow is the true object while the thin line represents the estimated boundary.

is given in Table I. The correlation regularization reduces E_{L^2} for the photoelectric image reconstruction roughly by a factor of three.

For the second example the background noise is increased so that SNR was 40dB. Results are demonstrated in Fig. 8. Error in the photoelectric image reconstruction increased compared to the previous example where SNR was 60dB. Nevertheless, the object boundaries are reconstructed quite accurately. Similar to previous case error levels in the reconstructions obtained with DEFBP method are high. Indeed, even for the Compton scatter image, the objects in the scene can hardly be distinguished by eye. See Table II for tabulated error values.

To construct the second phantom we took a DICOM image obtained from a CT scan of a duffel bag and imposed Compton scatter and photoelectric absorption coefficients so that the circular object close to middle was an object of interest and background was composed of low density clutter. The object of interest characteristics are set as the following: $c_0 = 0.3$, $\sigma_c = 0.05$, $p_0 = 5000$, $\sigma_p = 500$. Other parameters of the reconstruction scheme are kept the same as the previous example. We performed the simulation with 40dB background noise. Results are shown
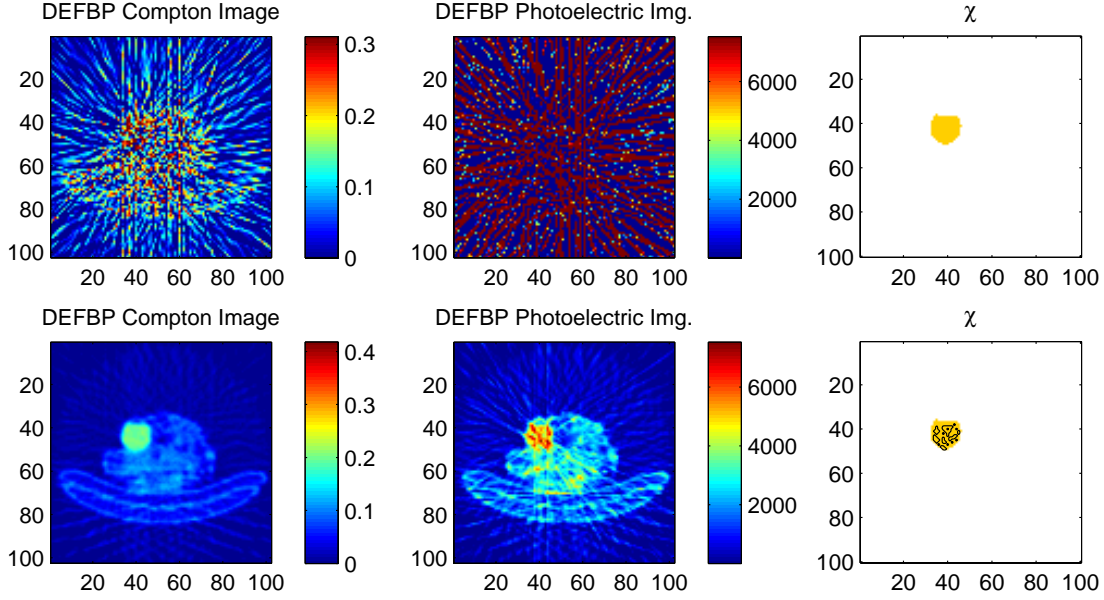
Fig. 10. Simulation with the duffle bag phantom with 40dB background noise. First row: DEFPB reconstruction. Second row: DEFPB reconstruction without background noise. First column: Compton image. Second column: Photoelectric image. Third column: Characteristic function, χ, of the object. The solid yellow is the true object while the thin line represents the estimated boundary.

TABLE III

ERROR ANALYSIS FOR THE EXPERIMENT WITH THE DUFFLE BAG PHANTOM AND 40DB BACKGROUND NOISE

Method	E_{L^2} Compton	E_{L^2} photoelectric	D_{χ}
Proposed method	0.1365	0.1913	0.7468
Proposed method without R_2	0.1311	0.2971	0.6325
DEFBP	1.6702	678.99	0
DEFBP without b.ground noise.	0.1099	0.2258	0.5026

in Fig. 9, Fig. 10 and Table III.

In the last example we intend to validate our method in the case where there is no object of interest in the scene. We repeated the first simulation keeping all the parameters but the definition of object of interest characteristics unchanged. For the definition of Γ we used the following values: $c_0 = 0.12$, $\sigma_c = 0.05$, $p_0 = 3000$, $\sigma_p = 500$. The results are shown in Fig. 11. In this example E_{L^2} values for Compton and photoelectric images were 0.1046 and 0.1498 respectively. As a result of the absence of an object of interest in the scene the algorithm returns a null characteristic function. The results are demonstrated in Fig. 11 and Table IV.

VI. CONCLUSIONS

A novel semi-shape based polychromatic dual energy CT algorithm with an emphasis on detection of objects whose physical characteristics in terms of Compton scatter and photoelectric absorption coefficients are known to some degree is developed. The *a priori* knowledge about the object characteristics is incorporated into the
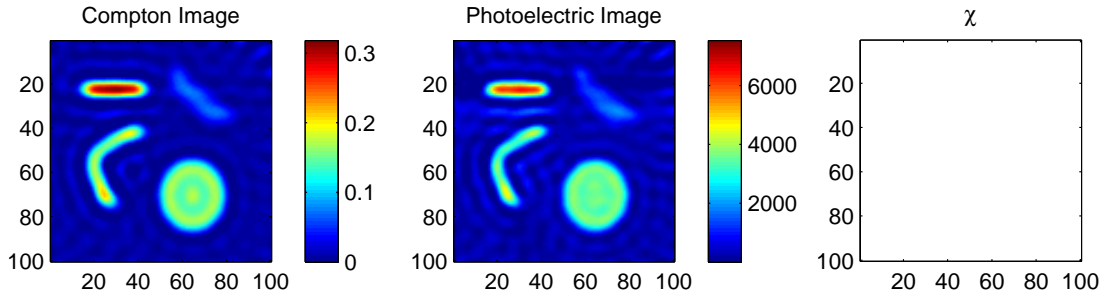
Fig. 11.   Simulation with the first phantom with 60dB background noise in the absence of object of interest. First column: Compton image. Second column: Photoelectric image. Third column: Characteristic function, χ, of the object. The solid yellow is the true object while the thin line represents the estimated boundary.

TABLE IV

ERROR ANALYSIS FOR THE EXPERIMENT WITH THE ABSENCE OF OBJECT OF INTEREST AND 60dB BACKGROUND NOISE

Method	E_{L^2} Compton	E_{L^2} photoelectric	D_χ
Proposed method	0.1046	0.1136	-

variational framework via constraints where Levenberg-Marquardt algorithm is used for minimization. Parametric level set approach where the level set function is described via low order basis expansion is implemented. This shape model is capable of representing various kinds of object geometries as shown in Section V. Along with object of interest boundaries the algorithm provides a reasonable reconstruction of the background images. With the proposed hybrid method we aim to increase the detection rate of objects of interest in an unknown cluttered background. As demonstrated in Section V accuracy of the photoelectric image reconstruction decreases as the background noise increases; however, object boundaries can still be recovered accurately. Similar to other level set based inverse problem methods, segmentation, hence detection, of the object of interest is simultaneously achieved with reconstruction of background images. This property is advantageous, for example, in airport security applications. Additionally, the use of the proposed correlation based regularization technique improves the reconstruction quality. This regularization technique can be used in inverse problem applications where different parameters, whose sensitivity to measurement data is vastly different, of the same scene needs to be simultaneously reconstructed and spatial similarity between those parameters is expected.

In future work, we intend to test the algorithm in the presence of metals or similar highly attenuating objects that would increase inconsistencies in the measurement data. Low photon count simulations and limited view tomography are also of interest of our research and will be addressed in future work. Another goal is to extend the level set framework so that multiple object types can be assigned as object of interest and treated individually. Additionally, the basis set for the level-set function can be constructed more adaptively. For instance, the widths, the locations and the orientation of each element(blob) in the set can be allowed to change during optimization to achieve greater flexibility. Consideration of different types of basis functions such as compactly supported radial basis functions and

wavelets in the representation of the background images is also a promising extension of this work. Regularization parameters are assigned heuristically in this work. For a practically more sound and effective method an automatic determination of regularization parameters is desirable. Finally, in order to make our method applicable to real-sized problems, we will consider increasing the resolution and phantom diameter, therefore optimizing the source code in terms of computational speed-up.

APPENDIX

SENSITIVITY ANALYSIS OF THE BACKGROUND RECONSTRUCTION PROBLEM

In order to give the reader intuition about the problems in reconstructing the photoelectric absorption, we present a sensitivity analysis of the background estimation problem. We consider a linearized problem and additive Gaussian noise where we analyse the sensitivity of the reconstruction to small chances in the data. We assume no object of interest is present and consider the Jacobian matrices that correspond to background parameters for Compton scatter and photoelectric absorption. For sake of simplicity we further assume that the Jacobian matrix is full rank[2] and estimate the errors by the relevant diagonal components of the error covariance matrix of the minimum variance unbiased (MVU) estimator. We provide lower bounds for errors associated with photoelectric and Compton component estimation and show that the bound on the mean square error (MSE) for the latter is significantly smaller.

Assume we have the measurement model for the low energy spectra $S_L(E)$ as in (10). If we plug (17) and (18) into (10) and take the derivatives with respect to β_j and α_j, we obtain:

$$
\begin{aligned}
[\mathbf{J}_c]_{ij} &= \frac{\partial [\mathbf{m}_L]_i}{\partial \beta_j} \\
&= \frac{[\mathbf{A}]_{i*}[\mathbf{B}]_{*j}}{[\mathbf{m}_L]_i} \int S_L(E) f_{KN}(E) \exp\bigl(-f_{KN}(E)[\mathbf{A}]_{i*}\mathbf{B}\boldsymbol{\beta} \\
&\quad - f_p(E)[\mathbf{A}]_{i*}\mathbf{B}\boldsymbol{\alpha}\bigr) \mathrm{d}E
\end{aligned}
\tag{47}
$$

and

$$
\begin{aligned}
[\mathbf{J}_p]_{ij} &= \frac{\partial [\mathbf{m}_L]_i}{\partial \alpha_j} \\
&= \frac{[\mathbf{A}]_{i*}[\mathbf{B}]_{*j}}{[\mathbf{m}_L]_i} \int S_L(E) f_p(E) \exp\bigl(-f_{KN}(E)[\mathbf{A}]_{i*}\mathbf{B}\boldsymbol{\beta} \\
&\quad - f_p(E)[\mathbf{A}]_{i*}\mathbf{B}\boldsymbol{\alpha}\bigr) \mathrm{d}E.
\end{aligned}
\tag{48}
$$

The spectra $S_L(E)$ consists of M discrete energy levels, therefore we define the matrices $\mathbf{W}_\beta$ and $\mathbf{W}_\alpha$ with elements

$$
\begin{aligned}
[\mathbf{W}_\beta]_{ij} = S_L(E_j) \exp\bigl(&-f_{KN}(E_j)[\mathbf{A}]_{i*}\mathbf{B}\boldsymbol{\beta} \\
&- f_p(E_j)[\mathbf{A}]_{i*}\mathbf{B}\boldsymbol{\alpha}\bigr)
\end{aligned}
\tag{49}
$$

and

$$
\begin{aligned}
[\mathbf{W}_\alpha]_{ij} = S_L(E_j) \exp\bigl(&-f_{KN}(E_j)[\mathbf{A}]_{i*}\mathbf{B}\boldsymbol{\beta} \\
&- f_p(E_j)[\mathbf{A}]_{i*}\mathbf{B}\boldsymbol{\alpha}\bigr).
\end{aligned}
\tag{50}
$$

---

[2]The assumption is reasonable. For instance, in the first example given in Section V, the size of the Jacobian matrix associated with the data mismatch term is 5640×1354 and its rank was calculated as 1352.

Using an appropriate Newton-Cotes numerical integration rule [71] with a weight vector $\boldsymbol{\omega}$ we can rewrite (47) and (48) as

$$\mathbf{J}_c = \mathbf{D_1 R} \tag{51}$$

and

$$\mathbf{J}_p = \mathbf{D_2 R} \tag{52}$$

where $\mathbf{D_1} = \mathrm{diag}(\mathbf{W}_\beta \mathrm{diag}(\boldsymbol{\omega})\mathbf{f_{KN}})$, $\mathbf{D_2} = \mathrm{diag}(\mathbf{W}_\alpha \mathrm{diag}(\boldsymbol{\omega})\mathbf{f_p})$ and $[\mathbf{R}]_{ij} = [\mathbf{m}_L]_i^{-1}[\mathbf{A}]_{i*}[\mathbf{B}]_{*j}$. But since $\mathbf{D_1}$ and $\mathbf{D_2}$ are diagonal, hence invertible, we can write

$$\mathbf{J}_p = \mathbf{D}\mathbf{J_c} \tag{53}$$

where $\mathbf{D} = \mathbf{D_2}\mathbf{D_1}^{-1}$.

Now, we can perform a sensitivity analysis with the following linear system of equations

$$\mathbf{H}\mathbf{f} + \mathbf{n} = \delta\mathbf{m} \tag{54}$$

where $\mathbf{H} = [\mathbf{J_c} \quad \mathbf{D}\mathbf{J_c}]$, $\mathbf{f} = [\boldsymbol{\delta\beta} \quad \boldsymbol{\delta\alpha}]^T$. For simplicity here we assume additive white Gaussian noise $\mathbf{n} \sim \mathcal{N}(0, \mathbf{I}\sigma^2)$. With (54) we investigate how small changes in the measurement data are reflected to the inversion process in the presence of Gaussian noise. If $\mathbf{H} \in \mathbb{R}^{\mathbf{M}\times\mathbf{N}}$, is full rank, the MVU estimator [72] is given as

$$\hat{\mathbf{f}} = (\mathbf{H^T H})^{-1}\mathbf{H^T}\delta\mathbf{m} \tag{55}$$

with the associated error covariance matrix, $\mathrm{cov}(\mathbf{f} - \hat{\mathbf{f}}) = \mathrm{E}\{(\mathbf{f} - \hat{\mathbf{f}})(\mathbf{f} - \hat{\mathbf{f}})^T)\}$ given by

$$
\begin{aligned}
\mathrm{cov}(\mathbf{f} - \hat{\mathbf{f}}) &= \sigma^2(\mathbf{H^T H})^{-1} \\
&= \sigma^2\begin{bmatrix} \mathbf{H^T H} & \mathbf{H^T H} \\ \mathbf{H^T D H} & \mathbf{H^T D^2 H} \end{bmatrix}^{-1} \\
&= \sigma^2\begin{bmatrix} \boldsymbol{\Lambda}_1^{-1} & \boldsymbol{\Lambda}_2^{-1} \\ \boldsymbol{\Lambda}_3^{-1} & \boldsymbol{\Lambda}_4^{-1} \end{bmatrix}.
\end{aligned} \tag{56}
$$

The block matrixes $\boldsymbol{\Lambda}_1, \boldsymbol{\Lambda}_2, \boldsymbol{\Lambda}_3$ and $\boldsymbol{\Lambda}_4$ are obtained using the matrix inversion lemma [17]. The trace of the covariance matrix can be used to determine the quality of the estimator. Therefore, only $\boldsymbol{\Lambda}_1$ and $\boldsymbol{\Lambda}_4$ be of interest and each is given as

$$\boldsymbol{\Lambda}_1 = \mathbf{H^T H} - \mathbf{H^T D H}(\mathbf{H^T D^2 H})^{-1}\mathbf{H^T D H} \tag{57}$$

and

$$\boldsymbol{\Lambda}_4 = \mathbf{H^T D^2 H} - \mathbf{H^T D H}(\mathbf{H^T H})^{-1}\mathbf{H^T D H}. \tag{58}$$

For the estimates $\widehat{\boldsymbol{\delta\beta}}$ and $\widehat{\boldsymbol{\delta\alpha}}$ we have the estimation errors $\mathrm{Tr}(\boldsymbol{\Lambda}_1^{-1})$ and $\mathrm{Tr}(\boldsymbol{\Lambda}_4^{-1})$ respectively. Now, the aim is to provide lower bounds for these traces. To start, define $\mathbf{M} = \mathbf{D H}$ and consider the reduced singular value decomposition (SVD) of $\mathbf{M}$ as $\mathbf{M} = \mathbf{U}_M\boldsymbol{\Sigma}_M\mathbf{V}_M^T$ and of $\mathbf{H}$ as $\mathbf{H} = \mathbf{U}\boldsymbol{\Sigma}\mathbf{V^T}$. We can write

$$\boldsymbol{\Lambda}_1^{-1} = \mathbf{V}\boldsymbol{\Sigma}^{-1}(\mathbf{I} + \mathbf{K}\mathbf{K}^T)^{-1}\boldsymbol{\Sigma}^{-1}\mathbf{V}^T \tag{59}$$

and

$$\mathbf{\Lambda}_4^{-1} = \mathbf{V}_M \mathbf{\Sigma}_M^{-1} (\mathbf{I} + \mathbf{KK}^T)^{-1} \mathbf{\Sigma}_M^{-1} \mathbf{V}_M^T \tag{60}$$

where $\mathbf{K} = \mathbf{U}^\mathbf{T} \mathbf{U}_\mathbf{M} \in \mathbb{R}^{\mathbf{M} \times \mathbf{N}}$. Since $\mathbf{V}$ is orthogonal, $\mathbf{\Lambda}_1^{-1}$ and $\mathbf{\Sigma}^{-1}(I + \mathbf{KK}^\mathbf{T})^{-1} \mathbf{\Sigma}^{-1}$ are similar. Likewise, $\mathbf{\Lambda}_4^{-1}$ and $\mathbf{\Sigma}_M^{-1}(\mathbf{I} + \mathbf{KK}^\mathbf{T})^{-\mathbf{1}} \mathbf{\Sigma}_\mathbf{M}^{-\mathbf{1}}$ are similar. Hence, the traces of $\mathbf{\Lambda}_1^{-1}$ and $\mathbf{\Lambda}_4^{-1}$ can be written in terms of these similar matrices as

$$E_{\boldsymbol{\beta}} = \mathrm{tr}\left[\mathbf{\Sigma}^{-1}(\mathbf{I} + \mathbf{KK}^\mathbf{T}) \mathbf{\Sigma}^{-\mathbf{1}} \right] \tag{61}$$

and

$$E_{\boldsymbol{\alpha}} = \mathrm{tr}\left[\mathbf{\Sigma}_M^{-1}(\mathbf{I} + \mathbf{K}^\mathbf{T}\mathbf{K}) \mathbf{\Sigma}_\mathbf{M}^{-\mathbf{1}} \right]. \tag{62}$$

Let us define $m_i = [\mathbf{I} + \mathbf{KK}^\mathbf{T}]_{ii} = [\mathbf{I} + \mathbf{K}^\mathbf{T}\mathbf{K}]_{ii}$. Now, we have

$$E_{\boldsymbol{\beta}} = \sum_{i=1}^N \frac{m_i}{\sigma_i^2(\mathbf{H})} \geq \min(m_i) \sum_{i=1}^N \frac{1}{\sigma_i^2(\mathbf{H})} \tag{63}$$

and

$$E_{\boldsymbol{\alpha}} = \sum_{i=1}^N \frac{m_i}{\sigma_i^2(\mathbf{DH})} \geq \min(m_i) \sum_{i=1}^N \frac{1}{\sigma_i^2(\mathbf{DH})}. \tag{64}$$

But, we can write

$$\begin{aligned}
\sum_{i=1}^N \frac{1}{\sigma_i^2(\mathbf{DH})} &= \frac{\sum_{i=1}^N \left(\prod_{k \neq i} \sigma_k^2(\mathbf{DH}) \right)}{\prod \sigma_k^2(\mathbf{DH})} \\
&= \frac{\sigma_1^2(\mathbf{DH})}{\sigma_1^2(\mathbf{DH})} \frac{\sum_{i=1}^N \left(\prod_{k \neq i} \sigma_k^2(\mathbf{DH}) \right)}{\prod \sigma_k^2(\mathbf{DH})} \\
&\geq \frac{N \prod \sigma_k^2(\mathbf{DH})}{\sigma_1^2(\mathbf{DH}) \prod \sigma_\mathbf{k}^\mathbf{2}(\mathbf{DH})} = \frac{N}{\sigma_1^2(\mathbf{DH})}
\end{aligned}$$

here $\sigma_1(\mathbf{DH})$ is the largest singular value of $\mathbf{DH}$. If we plug (65) into (64) we get

$$E_{\boldsymbol{\alpha}} \geq \frac{N \min(m_i)}{\sigma_1^2(\mathbf{DH})}. \tag{65}$$

Similarly, for $E_{\boldsymbol{\beta}}$ we have

$$E_{\boldsymbol{\beta}} \geq \frac{N \min(m_i)}{\sigma_1^2(\mathbf{H})}. \tag{66}$$

Next, we use the following inequality [73] for the largest singular value of a matrix $\mathbf{H}$

$$\sigma_1(\mathbf{H}) \leq \left[\|\mathbf{H}\|_\mathbf{1} \|\mathbf{H}\|_\infty \right]^{\mathbf{1/2}}. \tag{67}$$

Using (67) we can write

$$\sigma_1(\mathbf{DH}) \leq \|\mathbf{DH}\|_\mathbf{1} \|\mathbf{DH}\|_\infty \leq \mathrm{d}_{\max}^\mathbf{2} \left(\|\mathbf{H}\|_\mathbf{1} \|\mathbf{H}\|_\infty \right) \tag{68}$$

where, $d_{\max}$ is max $([D]_{ii})$. Now, (66) and (65) becomes

$$E_{\boldsymbol{\alpha}} \geq \frac{N \min(m_i)}{d_{\max}^2 \left(\|\mathbf{H}\|_\mathbf{1} \|\mathbf{H}\|_\infty \right)} \tag{69}$$

and

$$E_{\boldsymbol{\beta}} \geq \frac{N \min(m_i)}{\|\mathbf{H}\|_\mathbf{1} \|\mathbf{H}\|_\infty}. \tag{70}$$

TABLE V

SENSITIVITY ANALYSIS

Material	p	c	$d_{\max}^{-2}$
Water	4939.2	0.1907	4.3841×10^5
Plexiglass	3670.1	0.2157	4.3841×10^5
Aluminium	72887.5	0.4547	7.7815×10^6

The lower bound of $E_{\boldsymbol{\alpha}}$ is $d_{\max}^{-2}$ times bigger than that of $E_{\boldsymbol{\beta}}$. Our aim is to compare these lower bounds; hence at this point, we can be more concrete. For instance, consider a homogeneous 20×20 cm area illuminated from angle $\phi = 0$ by a parallel beam of X-rays using the low energy spectra $S_L(E)$. For this set up, we performed calculations corresponding three different scenario where the medium is filled with water, plexiglass and aluminium. Photoelectric absorption and Compton scatter coefficients [16] of these materials and calculated $d_{\max}^{-2}$ values are given in Table A. For instance, in case the medium is water the value of d^{-2} is 4.3841×10^5 which is approximately 15 times bigger than than the ratio of the actual photoelectric absorption and Compton scatter coefficients. Also note that the difference between the lower bounds increases dramatically as the attenuation characteristics of the medium increases as in the case of aluminium.

The lower bound for the error made while estimating the perturbations in photoelectric absorption coefficients is significantly bigger than the error associated with the estimation of perturbations in Compton scatter coefficients. From this point of view, we expect a similar behavior in the original (nonlinear) problem especially since Gauss-Newton (e.g., Levenberg-Marquardt) type algorithms rely on linearization of the problem at the current estimate to find the next estimate at each iteration. We can, therefore, conclude that photoelectric image reconstruction is more prone to error compared Compton image reconstruction. In this work we tried to address this issue using the regularization term given in (30).

ACKNOWLEDGMENT

REFERENCES

[1] P. Engler and W. Friedman, "Review of dual-energy computed tomography techniques," *Materials Evaluation*, vol. 48, pp. 623–629, 1990.

[2] T. Johnson, B. Krauß, M. Sedlmair, M. Grasruck, H. Bruder, D. Morhard, C. Fink, S. Weckbach, M. Lenhard, B. Schmidt *et al.*, "Material differentiation by dual energy CT: initial experience," *European radiology*, vol. 17, no. 6, pp. 1510–1517, 2007.

[3] S. Achenbach, K. Anders, and W. Kalender, "Dual-source cardiac computed tomography: image quality and dose considerations," *European radiology*, vol. 18, no. 6, pp. 1188–1198, 2008.

[4] H. Kröger, A. Kotaniemi, P. Vainio, and E. Alhava, "Bone densitometry of the spine and femur in children by dual-energy x-ray absorptiometry," *Bone and mineral*, vol. 17, no. 1, pp. 75–85, 1992.

[5] Z. Ying, R. Naidu, and C. Crawford, "Dual energy computed tomography for explosive detection," *J. of X-ray Sci. and Tech.*, vol. 14, no. 4, pp. 235–256, 2006.

[6] R. Alvarez and A. Macovski, "Energy-selective reconstructions in x-ray computerized tomography," *Phys. Med. Biol.*, vol. 21, no. 5, pp. 733–744, 1976.

[7] L. Lehmann, R. Alvarez, A. Macovski, W. R. Brodyand, N. J. Pelc, S. J. Rieder, and A. L. Hall, "Generalized image combinations in dual kvp digital radiography," *Med. Phys*, no. 5, 1981.

[8] W. A. Kalender, W. H. Perman, J. R. Vetter, and E. Klotz, "Evaluation of a prototype dual-energy computed tomographic apparatus. i. phantom studies," *Medical Physics*, vol. 13, no. 3, pp. 334–339, 1986.

[9] G. Zhang, J. Cheng, L. Zhang, Z. Chen, and Y. Xing, "A practical reconstruction method for dual energy computed tomography," *J. of X-ray Sci. and Tech.*, vol. 16, no. 2, pp. 67–8867–88, 2008.

[10] K. Goh, S. Liew, and B. Hasegawa, "Correction of energy-dependent systematic errors in dual-energyX-ray CT using a basis material coefficients transformation method," *IEEE Transactions on Nuclear Science*, vol. 44, no. 6 Part 2, pp. 2419–2424, 1997.

[11] J. Williamson, S. Li, S. Devic, B. Whiting, and F. Lerma, "On two-parameter models of photon cross sections: Application to dual-energy CT imaging," *Medical physics*, vol. 33, p. 4115, 2006.

[12] B. Heismann, "Atomic number measurement precision of spectral decomposition methods for ct," in *IEEE Nuclear Sci. Symp. Conf.*, 2005.

[13] P. Joseph and R. Spital, "A method for correcting bone induced artifacts in computed tomography scanners," *Journal of computer assisted tomography*, vol. 2, no. 1, p. 100, 1978.

[14] P. Sukovic and N. H. Clinthorne, "Penalized weighted least-squares image reconstruction for dual energy x-ray transmission tomography," *IEEE Trans. Med. Imag.*, vol. 19, no. 11, pp. 1075–1081, Nov. 2000.

[15] W. Kalender, E. Klotz, and L. Kostaridou, "An algorithm for noise suppression in dual energy CT material density images," *Medical Imaging, IEEE Transactions on*, vol. 7, no. 3, pp. 218–224, 2002.

[16] B. De Man, J. Nuyts, P. Dupont, G. Marchal, and P. Suetens, "An iterative maximum-likelihood polychromatic algorithm for CT," *IEEE transactions on medical imaging*, vol. 20, no. 10, pp. 999–1008, 2001.

[17] J. Kaipio and E. Somersalo, "Statistical and computational inverse problems," 2005.

[18] C. Markham and J. Fryar, "Element specific imaging in computerised tomography using a tube source of X-rays and low energy-resolution detector system," *Nuclear Instruments and Methods in Physics Research A*, vol. 324, pp. 383–388, 1993.

[19] G. Michael, "Tissue analysis using dual energy CT." *Australasian physical & engineering sciences in medicine/supported by the Australasian College of Physical Scientists in Medicine and the Australasian Association of Physical Sciences in Medicine*, vol. 15, no. 1, p. 25, 1992.

[20] P. S. N. H. C. J.A. Fessler, I. Elbakri, "Maximum-likelihood dual-energy tomographic image reconstruction," *SPIE Med. Imag.*, vol. 4684, no. 2, pp. 38–49, 2002.

[21] Z. Ying, R. Naidu, K. Guilbert, D. Schafer, and C. Crawford, "Dual energy volumetric x-ray tomographic sensor for luggage screening," in *Sensors Applications Symposium, 2007. SAS'07. IEEE.* IEEE, 2007, pp. 1–6.

[22] V. Butler, R. Poole, R. Foundation, and R. P. P. Institute, *Rethinking checked-baggage screening*. Reason Public Policy Institute, 2002.

[23] S. Singh and M. Singh, "Explosives detection systems (EDS) for aviation security," *Signal Processing*, vol. 83, no. 1, pp. 31–55, 2003.

[24] F. Lárusson, "Hyperspectral Imaging for Diffuse Optical Tomography," Ph.D. dissertation, Tufts University, 2009.

[25] L. Gallardo and M. Meju, "Characterization of heterogeneous near-surface materials by joint 2D inversion of dc resistivity and seismic data," *Geophys. Res. Lett*, vol. 30, no. 13, p. 1658, 2003.

[26] S. Osher and J. A. Sethian, "Fronts propagating with curvature dependent speed: Algorithms based on hamilton-jacobi formulations," *Journal of Computational Physics*, vol. 79, pp. 12–49, 1988.

[27] T. F. Chan and L. A. Vese, "Active contours without edges," *IEEE Trans. Image Process.*, vol. 10, no. 2, pp. 266–277, Feb. 2001.

[28] C. Samson, L. Blanc-Fraud, G. Aubert, and J. Zerubia, "A level set model for image classification," *Int. J. Comput. Vis.*, vol. 40, no. 3, pp. 187–197, 2000.

[29] A. Tsai, J. Yezzi, A., and A. Willsky, "Curve evolution implementation of the mumford-shah functional for image segmentation, denoising, interpolation, and magnification," *IEEE Trans. Image Process.*, vol. 10, no. 8, pp. 1169–1186, 2001.

[30] F. Santosa, "A level-set approach for inverse problems involving obstacles," *ESAIM Contrle Optim. Calc. Var*, vol. 1, pp. 17–33, 1996.

[31] O. Dorn and D. Lesselier, "Level set methods for inverse scattering," *Inverse Problems*, vol. 22, no. 4, pp. R67–R131, 2006.

[32] M. K. B. H. Miled and E. L. Miller, "A projection-based level-set approach to enhance conductivity anomaly reconstruction in electrical resistance tomography," *Inverse Problems*, vol. 23, no. 6, pp. 2375–2400, 2007.

[33] H. Feng, W. Karl, D. Castanon, M. Inc, and M. Natick, "A curve evolution approach to object-based tomographic reconstruction," *IEEE Transactions on Image Processing*, vol. 12, no. 1, pp. 44–57, 2003.

[34] V. Kolehmainen, M. Lassas, and S. Siltanen, "Limited data X-ray tomography using nonlinear evolution equations," *SIAM Journal on Scientific Computing*, vol. 30, no. 3, pp. 1413–1429, 2008.

[35] A. Aghasi, M. Kilmer, and E. Miller, "Parametric Level Set Methods for Inverse Problems," *Arxiv preprint arXiv:1007.2467*, to appear in SIAM Journal on Imaging Sciences.

[36] M. Kilmer, E. Miller, M. Enriquez, and D. Boas, "Cortical constraint method for diffuse optical brain imaging," in *Proceedings of SPIE*, vol. 5559, 2004, p. 381.

[37] L. R M, "Alternatives to voxels for image representation in iterative reconstruction algorithms," *Phys. Med. Biol*, vol. 37, p. 705, 1992.

[38] O. Bernard, D. Friboulet, P. Thevenaz, and M. Unser, "Variational b-spline level-set: A linear filtering approach for fast deformable model evolution," *IEEE Trans. Image Process.*, vol. 18, no. 6, pp. 1179–1191, Jun. 2009.

[39] G. Pingen, M. Waidmann, A. Evgrafov, and K. Maute, "A parametric level-set approach for topology optimization of flow domains," *Structural and Multidisciplinary Optimization*. [Online]. Available: http://dx.doi.org/10.1007/s00158-009-0405-1

[40] M. Wang, X. Wang, and D. Guo, "A level set method for structural topology optimization," *Computer Methods in Applied Mechanics and Engineering*, vol. 192, no. 1-2, pp. 227–246, 2003.

[41] A. Gelas, O. Bernard, D. Friboulet, and R. Prost, "Compactly supported radial basis functions based collocation method for level-set evolution in image segmentation," *IEEE Transactions on Image Processing*, vol. 16, no. 7, p. 1873, 2007.

[42] J. Beutel, M. Sonka, and J. Fitzpatrick, *Handbook of medical imaging*. Society of Photo Optical, 2000.

[43] P. Evans, "SpekCalc: a program to calculate photon spectra from tungsten anode x-ray tubes," *PHYSICS IN MEDICINE AND BIOLOGY*, vol. 54, no. 19, pp. N433–N438, 2009.

[44] G. Poludniowski and P. Evans, "Calculation of x-ray spectra emerging from an x-ray tube. Part I. Electron penetration characteristics in x-ray targets," *Medical Physics*, vol. 34, p. 2164, 2007.

[45] G. Poludniowski, "Calculation of x-ray spectra emerging from an x-ray tube. Part II. X-ray production and filtration in x-ray targets," *Medical Physics*, vol. 34, p. 2175, 2007.

[46] I. Elbakri and J. Fessler, "Segmentation-free statistical image reconstruction," *Physics in Medicine and Biology*, vol. 48, pp. 2453–2477, 2003.

[47] V. Hansen, W. Swindell, and P. Evans, "Extraction of primary signal from EPIDs using only forward convolution," *Medical Physics*, vol. 24, p. 1477, 1997.

[48] P. Joseph and R. Spital, "The effects of scatter in x-ray computed tomography," *Medical physics*, vol. 9, p. 464, 1982.

[49] B. De Man, J. Nuyts, P. Dupont, G. Marchal, and P. Suetens, "Metal streak artifacts in X-ray computed tomography: a simulation study," *IEEE Transactions on Nuclear Science*, vol. 46, no. 3, pp. 691–696, 1999.

[50] J. Tang, B. Nett, and G. Chen, "Performance comparison between total variation (TV)-based compressed sensing and statistical iterative reconstruction algorithms," *Physics in Medicine and Biology*, vol. 54, pp. 5781–5804, 2009.

[51] D. Wiegert and U. Ohm, *Scattered radiation in cone-beam computed tomography: analysis, quantification and compensation*. Citeseer, 2007.

[52] S. Osher and R. P. Fedkiw, *Level Set Methods and Dynamic Implicit Surfaces, Applied Mathematical Sciences*. New York: Springer, 2002, vol. 153.

[53] O. Dorn, E. Miller, and C. Rappaport, "A shape reconstruction method for EM tomography," *Inverse problems*, vol. 16, pp. 1119–1156, 2000.

[54] M. Schweiger and S. Arridge, "Image reconstruction in optical tomography using local basis functions," *Journal of Electronic Imaging*, vol. 12, p. 583, 2003.

[55] C. Bouman and K. Sauer, "A unified approach to statistical tomography using coordinate descent optimization," *Image Processing, IEEE Transactions on*, vol. 5, no. 3, pp. 480–492, 1996.

[56] S. Siltanen, V. Kolehmainen, S. Järvenpää, J. Kaipio, P. Koistinen, M. Lassas, J. Pirttilä, and E. Somersalo, "Statistical inversion for medical x-ray tomography with few radiographs: I. General theory," *Physics in Medicine and Biology*, vol. 48, p. 1437, 2003.

[57] B. Whiting, P. Massoumzadeh, O. Earl, J. OSullivan, D. Snyder, and J. Williamson, "Properties of preprocessed sinogram data in x-ray computed tomography," *Medical Physics*, vol. 33, p. 3290, 2006.

[58] P. Massoumzadeh, O. Earl, and B. Whiting, "Noise simulation in x-ray CT," in *Proc. SPIE*, vol. 5745, 2005, pp. 898–909.

[59] V. Kolehmainen, S. Siltanen, S. Järvenpää, J. Kaipio, P. Koistinen, M. Lassas, J. Pirttilä, and E. Somersalo, "Statistical inversion for medical x-ray tomography with few radiographs: II. Application to dental radiology," *Physics in Medicine and Biology*, vol. 48, p. 1465, 2003.

[60] M. Berger, J. Hubbell, S. Seltzer, J. Chang, J. Coursey, R. Sukumar, and D. Zucker, "Xcom: Photon cross section database (version 1.3)," *National Institute for Standards and Technology*, 2005.

[61] L. Gallardo, M. Meju, and M. Pérez-Flores, "A quadratic programming approach for joint image reconstruction," *Inverse Problems*, vol. 21, pp. 435–452, 2005.

[62] M. Belge, M. Kilmer, and E. Miller, "Efficient determination of multiple regularization parameters in a generalized L-curve framework," *Inverse Problems*, vol. 18, no. 4, pp. 1161–1183, 2002.

[63] G. Golub, M. Heath, and G. Wahba, "Generalized cross-validation as a method for choosing a good ridge parameter," *Technometrics*, vol. 21, no. 2, pp. 215–223, 1979.

[64] V. Morozov, Z. Nashed, and A. Aries, *Methods for solving incorrectly posed problems*.   Springer New York, 1984.

[65] D. Luenberger and Y. Ye, *Linear and nonlinear programming*.   Springer Verlag, 2008.

[66] H. Yamashita and T. Tanabe, "A primal-dual exterior point method for nonlinear optimization," *SIAM Journal on Optimization*, 2007.

[67] R. Fletcher, "Practical Methods of Optimization: Vol. 2: Constrained Optimization." *JOHN WILEY & SONS, INC., ONE WILEY DR., SOMERSET, N. J. 08873, 1981, 224*, 1981.

[68] R. Byrd, J. Nocedal, and R. Waltz, "Steering exact penalty methods for nonlinear programming," *Optimization Methods and Software*, vol. 23, no. 2, pp. 197–213, 2008.

[69] D. Marquardt, "An algorithm for least-squares estimation of nonlinear parameters," *Journal of the Society for Industrial and Applied Mathematics*, pp. 431–441, 1963.

[70] K. Madsen, H. Bruun, and O. Imm, "Methods for non-linear least squares problems," 2004.

[71] K. Atkinson, *An introduction to numerical analysis*.   Wiley-India, 2009.

[72] S. Kay, *Fundamentals of Statistical signal processing, Volume 2: Detection theory*.   Prentice Hall PTR, 1998.

[73] R. Horn and C. Johnson, *Topics in matrix analysis*.   Cambridge Univ Pr, 1994.